To the Graduate Council:

I am submitting herewith a thesis written by Bruce Edwin Murphree entitled "The Kinetics of the Steam Activation of Coal Char". I recommend that it be accepted in partial fulfillment of the requirements for the degree of Master of Science, with a major in Chemical Engineering.

Donald C. Bogue

Donald C. Bogue, Chairman of Committee

We have read this thesis
and recommend its acceptance:

George C. Frazier

H. W. Haas

J. S. Watson

Accepted for the Council:

L. Evans Roth

Vice Chancellor
Graduate Studies and Research

Thesis
77
M275

THE KINETICS OF THE STEAM ACTIVATION OF COAL CHAR

A Thesis

Prepared for the

Master of Science

Degree

The University of Tennessee, Knoxville

Bruce Edwin Murphree

August 1977

1328503

ACKNOWLEDGEMENTS

This research was carried out at the Department of Chemical Engineering, Kyoto University, Kyoto, Japan, under the direction of Professor Kenji Hashimoto, as part of a special program between The University of Tennessee, Knoxville and Kyoto University. Under this program degree candidates carry out their course work at The University of Tennessee, Knoxville and their research work at Kyoto University.

Special thanks is given to Professor Kenji Hashimoto for his aid in making the arrangements for the "Year-In-Japan" program and for his direction of the research at Kyoto University. Also the financial support from the Ministry of Education of Japan, while I was in Japan, is acknowledged with thanks.

I also would like to thank Dr. Donald C. Bogue for his continued assistance with the "Year-In-Japan" program and for his guidance in the writing of this thesis.

Finally, I would like to express my personal thanks to Miura Kouchi and his wife for their kindness shown toward my wife and I during our stay in Japan. Also, I would like to express special thanks to my wife for all the assistance she gave in the typing and finalizing of this thesis.

ABSTRACT

The kinetics of the steam activation of coal chars was studied experimentally and a theoretical model involving the micropore and macropore structure was developed. Two types of coal char, one pelletized (Miike) and the other non-pelletized (Victoria), were reacted with steam at a total pressure of one atmosphere and the weight loss was continuously recorded using a micro-balance system.

A series of experiments was conducted at atmospheric pressure to obtain the kinetic data. Three different temperatures (750°C, 800°C, and 850°C) and four partial pressures of steam (0.1 atm. to 1.0 atm., with N_2 as the inert gas) were used in the micro-balance apparatus to obtain the rate data for the two coal chars. These data were combined with the pore structure data from a fluidized bed obtained by other investigators.

The model, which separated the pore structure into micropores and macropores, was developed by using a "population balance" equation for the creation and destruction of pores and by assuming that the rate was kinetically controlled. The latter assumption was substantiated by the independence of the reaction rate data on the change in particle diameter. The model was able to fit both the rate and pore structure data.

The micropore gasification rate was found to be independent of the surface area, which indicated that the rate of micropore initiation was much greater that the rate of micropore growth. The initiation rate constants and activation energies for the pelletized and non-pelletized coal char were very similar, indicating that the initiation mechanism is probably the same within a given group of coal chars. The macropore rate and development were affected by the pelletizing and were dependent upon the

surface area. This was related to the catalytic effect of the ash from the binder.

TABLE OF CONTENTS

CHAPTER		PAGE
I.	INTRODUCTION	1
II.	BACKGROUND AND DEVELOPMENT OF THEORETICAL MODELS	4
	Activation of Carbonaceous Material	4
	Theoretical Framework for Modeling Carbon Pore Structure	7
	Development of a Combined Micropore and Macropore Model	13
III.	EXPERIMENTAL	19
	Apparatus	19
	Sample Materials	22
	Procedure	23
	System Characterization and Preliminary Tests	25
IV.	RESULTS AND DISCUSSION	33
	Summary of Data from the Micro-Balance	33
	Summary of Equations and Determination of Parameters	38
	Comparison of the Final Equations to the Measured Variables	50
V.	CONCLUSIONS AND RECOMMENDATIONS	68
	Conclusions	68
	Recommendations	69
LIST OF REFERENCES		71
APPENDICES		74
APPENDIX A.	DEVELOPMENT OF THE EQUATIONS FOR THE COMBINED MODELS	75

PAGE

APPENDIX B. EQUIPMENT SPECIFICATIONS 82

APPENDIX C. CALCULATION OF THE EFFECTIVENESS FACTOR 83

APPENDIX D. SCANNING ELECTRON MICROGRAPHS 86

VITA 88

LIST OF TABLES

TABLE		PAGE
3.1.	Composition of Coal Char	23
3.2.	System Characterization Experiments for the Micro-Balance Using Overall Conversion Data for Pelletized Coal Char	27
3.3.	Micro-Balance Overall Conversion Data for Pelletized Coal	29
3.4.	Experimental Conditions for Micro-Balance Experiments with Pelletized Coal Char	30
3.5.	Pore Development Comparison Between the Micro-Balance and the Fluidized Bed	32
4.1.	Micro-Balance Overall Conversion Data for Non-Pelletized Coal Char	34
4.2.	Experimental Conditions for Micro-Balance Experiments with Non-Pelletized Coal Char	35
4.3.	Pore Structure Data for Pelletized Coal Char	36
4.4.	Pore Structure Data for Non-Pelletized Coal Char	37
4.5.	Parameters Determined from Initial Data	43
4.6.	Parameters Determined from Non-Linear Least Squares Analysis of the Rate and Pore Structure Data	47
C-1.	Effectiveness Factors for the Pelletized Material	85

LIST OF FIGURES

FIGURE		PAGE
2.1.	Crystalline Structure of Graphite	9
3.1.	Experimental Apparatus	20
3.2.	Low Partial Pressure Steam Apparatus	21
3.3.	Gasification Experiment on the Micro-Balance Apparatus.	26
4.1.	Arrhenius Plot for Micropore Initiation Rate Constant	46
4.2.	Arrhenius Plot for Macropore Rate Constant	49
4.3.	Micropore Conversion for Pelletized Coal	51
4.4.	Micropore Conversion for Non-Pelletized Coal	52
4.5.	Internal Conversion for Pelletized Coal	54
4.6.	Internal Conversion for Non-Pelletized Coal	55
4.7.	Overall Conversion for Pelletized Coal	58
4.8.	Overall Conversion for Non-Pelletized Coal	59
4.9.	Micropore Conversion versus Overall Conversion	61
4.10.	Relative Micropore Surface Area versus Overall Conversion	62
4.11.	Internal Conversion versus Overall Conversion	63
4.12.	Relative Macropore Volume versus Overall Conversion	64
4.13.	Relative Macropore Surface Area versus Overall Conversion	65
4.14.	Relative Macropore Length versus Overall Conversion	65
4.15.	Relative Particle Radius versus Overall Conversion	66
D-1.	Micrograph of the Pelletized Material at 50x	86
D-2.	Micrograph of the Non-Pelletized Material at 50x	87

NOMENCLATURE

- a - Subscript indicating macropore property
- A - Empirical constant used in equation 2.6
- B, B_f, B_c - Rate of introduction of new pores by initiation and combination
- B_n - Grouped coefficients
- C_a - Pre-exponential factor in equation 4.11
- C_g - Reactant concentration
- C_i - Pre-exponential factor in equation 4.12
- D - Rate of removal of pores by coalescence
- D_a - Effective diffusivity
- E_{aa} - Activation energy for macropore rate constant in equation 4.11
- E_{ai} - Activation energy for micropore initiation rate constant in equation 4.10
- F - External surface area correction factor
- $f(r)$ - Pore density distribution function
- i - Subscript indicating micropore property
- K - Dimensionless group in equation C-1
- K_a - Macropore growth rate constant
- K_i - Micropore growth rate constant
- K_f - Micropore initiation rate constant
- K_n - General reaction rate constant
- K_s - First order surface rate constnat in equation C-5
- $\overline{l}$ - Mean macropore length
- L_a - Specific macropore length
- M_B - Molecular weight of carbon
- M_n - nth moment

n - Moment subscript

P, P_i - Pressure, Partial Pressure

R, R_p - Particle radius

r_a - Macropore radius

r_c - Characteristic radius of a newly combined pore

r_f - Radius of an initiated pore

S - Specific surface area

S_a - Specific macropore surface area

S_i - Specific micropore surface area

s_i - Surface area of one crystallite layer

t - time

V_a - Specific macropore volume

V_i - Specific micropore volume

x - Conversion

x_f - Overall conversion

x_i - Micropore conversion

x_{oa} - Internal conversion

GREEK LETTERS

α - Linearization constant in equation 2.27

Γ - Relative surface area = S/S°

Γ_a - Relative macropore surface area = S_a/S_a°

Γ_i - Relative micropore surface area = S_i/S_i°

δ - Dirac delta function

ϵ_a - Proportionality constant for macropore combination function, equation 4.7

ϵ_i - Proportionality constant for micropore combination function, equation 4.6

ξ - Relative particle radius = R_p/R_p°

Λ_a - Relative macropore length = L_a/L_a°

η_e - Effectiveness factor

π - Pi

$\rho_B, \rho_{B_{oa}}$ - Apparent particle density

ρ_{B_i} - Apparent micropore density

ρ_t - True density

σ - Standard deviation

Φ, Φ^* - Relative pore combination rate function = ϕ/ϕ°

Φ_a^* - Relative macropore combination rate function = ϕ_a/ϕ_a°

Φ_i^* - Relative micropore combination rate function = ϕ_i/ϕ_i°

ϕ_a - Macropore combination rate function

ϕ_i - Micropore combination rate function

Ω_a - Relative macropore volume = V_a/V_a°

CHAPTER I

INTRODUCTION

In recent years there has been increasing interest in the ecological and environmental problems associated with industrial waste and municipal sewage. This means liquid and gaseous wastes must be cleaned to acceptable limits before releasing them into the environment. A number of cleaning methods are being developed, some of which employ activated carbon as the adsorbent.

Activated carbons have long been used as adsorbents.[8] The absorptive capacity of activated carbons greatly depends on their pore structure and surface area, therefore the producers of activated carbons must be able to predict these properties and to design activation reactors that will give the desired properties.

Reliable rate data are essential to the successful design of reactors.[18] A full understanding of the kinetics and mechanisms of the reactions is necessary for the proper modeling of the rate data. There are three general activation reactions:

$$2C_{(s)} + O_2 \rightleftharpoons 2CO_{(g)} \qquad 1.1$$

$$C_{(s)} + CO_2 \rightleftharpoons 2CO_{(g)} \qquad 1.2$$

$$C_{(s)} + H_2O_{(g)} \rightleftharpoons CO_{(g)} + H_{2(g)} \qquad 1.3$$

The activation using O_2, as will be noted in more detail later, results in a highly exothermic reaction and thus is not a common industrial process. Either reaction 1.2 or 1.3, or a combination of the two, is most commonly used.

Early work was done by Petersen[9] and Thomas[15]. They only considered the microscopic changes in pore size. Hashimoto and Silveston[4,5] and Schechter and Gidley[12] applied the population balance technique to porous material. Hashimoto and Silveston applied their model to the activation of devolatized anthracite by carbon dioxide. They investigated the two general isothermal cases of either kinetically controlled[4] or diffusion controlled[5] processes. Their model has been expanded to include activation by steam and some reactivation reactions. Schechter and Gidley[12] applied their model to the reaction of dilute hydrochloric acid on limestone.

These models for predicting the properties of activated carbons gave the properties as a function of gasification or extent of reaction. This removed the time dependence from all the equations. However, for the successful design or scale-up of activation reactors one needs to consider the kinetics of the reaction.

The kinetics of oxidation reactions of carbon and the development of the pore structure have been investigated by many people. However, these mechanisms generally have been analyzed separately. Riede and Hanesian[11] in studying the reaction between graphite and steam used the external surface area of their sample. Most investigators agree that gas-carbon reactions are related to certain active sites on the carbon surface. If this is true the rate of reaction should be dependent upon the pore structure development.

The present thesis is concerned with the development of a kinetics model for coal char activation by steam. The kinetics model incorporates the pore structure of the material. The system is assumed to have a

bimodal pore distribution, where the micropore radius is less than 100Å and the macropores are greater than 100Å. The micropores are assumed to be slit shaped due to the crystallite structure and the macropores to be cylindrically shaped.

CHAPTER II

BACKGROUND AND DEVELOPMENT OF THEORETICAL MODELS

A. ACTIVATION OF CARBONACEOUS MATERIAL

There is a very wide range of starting materials for the production of activated carbons. Some of these include coconut shells, peach pits, sawdust, wood char, fish, lignit, petroleum coke, bone char, anthracite coal, coffee grounds, molasses, rice hulls, carbon black, peat, kelp and sugar. Essentially any carbonaceous material can be activated. It should be noted that whether a high carbon content material like carbon black is activated directly or whether some low carbon content material is charred and then activated does not appear to be important with respect to the surface chemistry.[8]

Before going further it is necessary to present some operational definitions of terms used in the process of activation.

Activation[8] refers to the overall process of producing an "active" carbon which is capable of chemically or physically adsorbing certain species from gas or liquid solutions. It may be used to refer to the process of heating a char to a sufficiently high temperature to cause the extensive burn-off of carbon impurities, leaving a high-surface area, highly porous product. The initial high-temperature treatment can be carried out with or without the presence of an oxident. If the heating step is carried out without oxidizing agents (O_2, CO_2, H_2O), it must be oxidized in order to yield an "active" product. This oxidation can occur by exposing the product to air during cooling. The sequence or nature of

the activation process does not matter, only the final extent of the oxidation of the surface.

Coking[8] refers to the process of heating the carbonized material in an inert (oxident free) atmosphere at a very high temperature (>1000 °C) in order to drive off all the non-carbon components, and using the material bound oxygen for "self-oxidation".

Charring[8] refers to the partial oxidation by burning of a starting material during heating. Charring is carried out to obtain material with a high carbon content (90% carbon), which may then be activated.

Oxidation[8] in the present context means exposing the carbonaceous material to oxidizing agents in the gas phase (O_2, CO_2, H_2O) at temperatures above 200 °C. The oxidation process is the most important with respect to the functional groups on the surface.

The most important step in the production of activated carbon is that of oxidation.[8] As noted in equations 1.1, 1.2 and 1.3 there are three general oxidizing reactions used in gasification techniques. The first reaction is the most obvious one, that involves oxygen directly:

$$C_{(s)} + O_2 \rightleftharpoons 2CO_{(g)}$$

This reaction in the temperature range of 600 °C to 800 °C is one-half order with respect to the partial pressure of oxygen (when the P_{O_2} is between 1 μ and 100 μ Hg).[1] This reaction is not often used in commercial operations because the heat of reaction is high (ΔH = -52.8 kcal/kg.mole), which makes the gasification hard to control. The second reaction involves the use of carbon dioxide as the oxidizing agent:

$$C_{(s)} + CO_2 \rightleftharpoons 2CO_{(g)}$$

This reaction proceeds by a two step mechanism. The carbon dioxide is chemisorbed on the surface, followed by the evolution of the carbon monoxide to the gas phase:[16]

$$C_{(s)} + CO_2 \rightleftharpoons CO_{(g)} + CO_{(s)}$$

$$CO_{(s)} \rightleftharpoons CO_{(g)} + nC_{(s)}$$

If "n" is unity then the number of reaction sites does not change. The Langmuir-type rate expression for the reaction is of the form:[16]

$$\text{RATE} = \frac{K_1 P_{CO_2}}{1 + K_2 P_{CO} + K_3 P_{CO_2}} \qquad 2.1$$

This is the general overall rate expression. When $K_2 P_{CO} << 1$, the kinetics of the reaction can be either first or zero order with respect to the carbon dioxide. This reaction is endothermic (ΔH = 41.5 kcal/kg.mole): it is used commercially, either by itself or with a mixture of carbon dioxide and steam. The third reaction is with steam:

$$C_{(s)} + H_2O \rightleftharpoons CO_{(g)} + H_2$$

The mechanism for this reaction is one involving two steps.[8] The water vapor is adsorbed onto the carbon surface, followed by the evolution of CO and H_2. The Langmuir-type rate expression for the reaction is of the form:

$$\text{RATE} = \frac{K_1 P_{H_2O}}{1 + K_2 P_{H_2O} + K_3 P_{H_2}} \qquad 2.2$$

The rate determining step is the desorption of the CO from the surface.[14] It should, therefore, have surface oxygen complexes similar to those produced when oxygen is used in the activation process. If $K_3P_{H_2} << 1$, equation 2.2 reduces to:

$$\text{RATE} = \frac{K_1 P_{H_2O}}{1 + K_2 P_{H_2O}} \qquad 2.3$$

Therefore, the reaction rate will be between zero and first order depending on the magnitude of $K_2P_{H_2O}$. This reaction is much easier to control than the reaction with oxygen because it is endothermic (ΔH = 24.0 kcal/kg.mole). Consequently, it is more widely used commercially.

During activation the main factor, as far as the surface chemistry is concerned, is the final extent of the oxidation of the surface.[8] Oxidation is not the only factor which can affect the adsorptive capability of activated carbons. The total surface area, the pore volume and the pore size distribution also affects the adsorptive properties of the final product. The adsorption of a material from solution is often limited by pore diffusion. Therefore, the pore structure of activated carbon plays a major part in characterizing its adsorptive performance. Consequently, work has been done to model the pore structure and its changes as a function of the extent of gasification.[3,4,9,15,17,19]

B. THEORETICAL FRAMEWORK FOR MODELING CARBON PORE STRUCTURE

Microscopic Models

Micropores in activated carbon are important with regard to the overall adsorption capability because almost all of the surface is accounted for in them. Many different shapes have been assumed for the structure

of the micropores. These have ranged from open or closed capillaries to ink-bottle-shaped or conical shaped[7,15], and slit shaped ones[13].

An early model by Thomas[15] assumed a conical shaped pore. He considered the possibility that the pore geometry could be related to the laminated graphite material. Hashimoto and Silveston[4,5] used a simple cylindrical shaped pore which was open on both ends. Their main contribution was the introduction of the population balance technique. This method allowed for the creation and destruction of pores by combination with surrounding pores. Their general equation is:[4]

$$\frac{\partial f}{\partial t} + \frac{\partial}{\partial r}\left(f \frac{dr}{dt}\right) - B + D = 0 \qquad 2.4$$

where, f, is a density distribution function, B is a rate term for the formation of new pores by initiation and combination, and D is the term for the coalescence of adjacent pores.

This model was simplified by Hashimoto and Miura[3] by assuming a slit shaped pore. The slit shaped pore approximation can be justified by examining the crystalline structure of activated carbon as was suggested by Thomas.[15]

The crystalline structure of activated carbon is similar to the structure of graphite. This structure is composed of layer planes of carbon atoms ordered in regular hexagons, similar to aromatic rings. The spacing of the carbon atoms within a single layer is 1.42Å and the layers are 3.34Å apart (See Figure 2.1).[13] However, the structure of activated carbon is less uniform than that of graphite. The parallel planes are not perfectly oriented. This orientation has been called a "turbostratic structure".[8] The overall dimensions of the crystallites depends on the

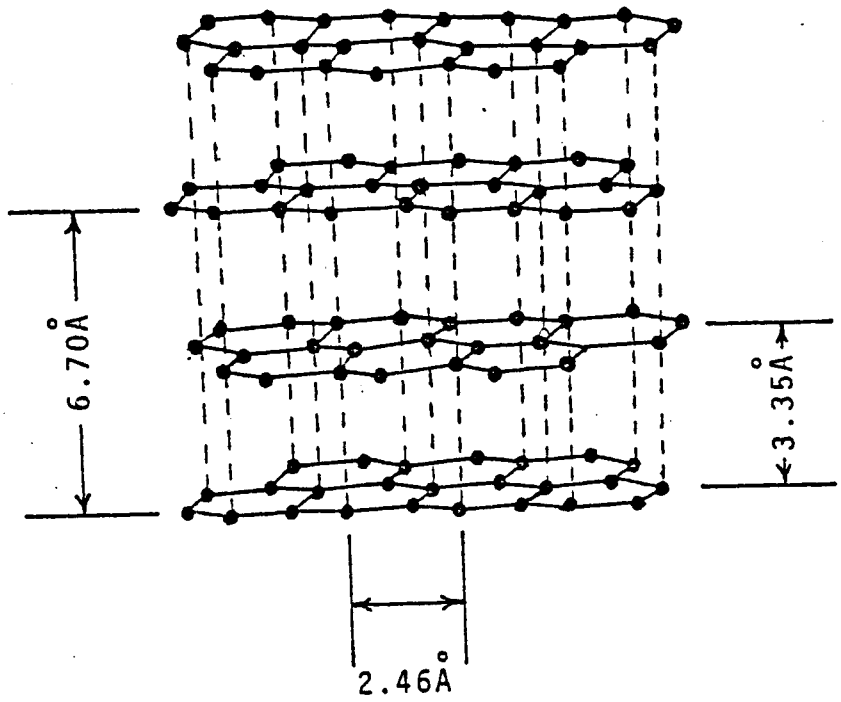


Figure 2.1. Crystalline Structure of Graphite.

carbonization temperature. The thickness is 4 to 12 layers (10Å to 37Å) and the diameter, if a circular cross section is assumed, is 20Å to 70Å.[13] These dimensions give the surface area of the micropore as twice the area of one layer ($314Å^2$ to $3850Å^2$) and the minimum radius would be half the layer spacing (r_m = 1.675Å). These two assumptions greatly reduced the mathematical complexity of the population balance equation. Hashimoto and Miura[3] assumed the reaction was first order with respect to the gas phase reactant. The rate of pore growth was:

$$\frac{dr}{dt} = \frac{K_1 M_B C_g}{\rho_t} \qquad 2.5$$

where the density, ρ_t, is the true density of the carbon matrix. The birth term in equation 2.4 had two parts, initiation and combination. The initiation term, B_f, was assumed kinetically similar to the pore growth and would have a characteristic radius, r_f, which was half the crystalline layer spacing (r_f = 1.675Å). Hashimoto and Silveston[4,5] made the relative pore combination probability function, Φ, an empirical function of conversion:

$$\Phi = Ax^B \qquad 2.6$$

where A and B were empirical constants. Schechter and Gidley[12] based it upon the rate of pore growth, which for their material is related to conversion. Hashimoto and Miura[3] compared the Hashimoto and Silveston[4,5] model (modified for slit shaped pores) with that of Schechter and Gidley[12] and obtained the relation:

$$\phi = 4s \frac{dr}{dt} = \frac{4sK_1 M_B C_g}{\rho_t} \qquad 2.7$$

This expression states that the combination probability function was a constant, which was inconsistant because they knew that it should increase with gasification. This was corrected by changing from the true density, ρ_t, to the apparent density, ρ_B, in the pore growth rate equation.

$$\frac{dr}{dt} = \frac{K_1 M_B C_g}{\rho_B} \qquad 2.8$$

This made the relative pore combination function, Φ^*, inversely proportional to the conversion.

$$\Phi^* = \frac{1}{(1-x)} \qquad 2.9$$

Using these assumptions they developed a new set of equations for the relative pore surface area, Γ, and conversion, x:

$$\frac{d\Gamma}{dt} = B_1 + B_2\Gamma - \left(1 - \frac{B_3}{(1-x)}\right)\Gamma^2 \qquad 2.10$$

$$\frac{dx}{dt} = B_3\Gamma + B_2 (1-x_i) \qquad 2.11$$

where $B_1 = \frac{2_s K_f C_g}{S^\circ}$,

$B_2 = 2sK_f \rho_t r_f C_g$ and,

$B_3 = \frac{\rho_t}{\rho_B} K_1 M_B S^\circ C_g$

Dividing equation 2.10 by equation 2.11 to eliminate time one obtains:

$$\frac{d\Gamma}{dx} = \frac{\Gamma}{(1-x)} + \frac{B_1 - \Gamma^2}{B_3\Gamma + B_2 (1-x)} \qquad 2.12$$

This was fitted to data obtained from the steam activation of coal char in a fluidized bed reactor.[6,20] The conversion, x, was obtained from the apparent density:

$$x = 1 - \rho_B / \rho_B^o \qquad 2.13$$

This approach worked reasonably well and was much simpler then the original model of Hashimoto and Silveston.[4,5]

Macroscopic Models

A macropore model was presented by Petersen for the gasification of porous graphite rods with carbon dioxide.[9] He modeled the porous solid as a set of cylindrical pores with random intersections. He also states that the macropores are the interstitial spaces between the graphite particles. The material was pelletized using coal-tar as a binder.

Schechter and Gidley[12] used a similar approach for their model of the change in the pore structure of limestone. Like Petersen, they assumed randomly dispersed cylindrical pores. However, they included the possibility of coalescence with surrounding pores. Also, they employed the population balance equation to handle the distribution of pore sizes. Their equation development is basically the same as that of Hashimoto and Silveston[4,5], with the exception that Schechter and Gidley based the pore combination function on the rate of pore growth and did not use and initiation term. Their model was compared with experimental data from the reaction of dilute hydrochloric acid on limestone. The model behaved in a similar manner as the real system.[12]

The reaction of limestone with acid is a somewhat simpler system than the activation of coal char. Coal char can have pores ranging from

a few Angstroms in radius to several thousand. It can be made to have a simple bimodal pore size distribution. With a bimodal pore size distribution, both micropores and macropores should be accounted for in developing a complete model.

C. DEVELOPMENT OF A COMBINED MICROPORE AND MACROPORE MODEL

The combined model assumes that the pore distribution can be divided into two distinct parts. The micropores were pores with a radius less than 100Å, and the macropores were pores with a radius greater than 100Å. By dividing the solid into two parts, the micropores can be treated separately from the macropores.

The overall internal conversion is the same as Hashimoto and Miura's[3] equation 2.13:

$$x_{oa} = 1 - \frac{\rho_{B_{oa}}}{\rho^{o}_{B_{oa}}} \qquad 2.13$$

where

$$\frac{1}{\rho_{B_{oa}}} = V_a + V_i + \frac{1}{\rho_t}$$

V_a, is the macropore volume and V_i is the micropore volume. Similarly, the apparent density of the carbon excluding all pores greater than 100Å can be used to calculate the micropore conversion:

$$x_i = 1 - \frac{\rho_{B_i}}{\rho^{o}_{B_i}} \qquad 2.14$$

and,

$$\frac{1}{\rho_{B_i}} = V_i + \frac{1}{\rho_t} \qquad 2.15$$

The micropores were modeled in the same manner as Hashimoto and Miura[3]. The pores were assumed to be slit shaped conforming to the crystalline structure. The basic moment equation was the same as Hashimoto and Miura, except that the conversion was only for the micropores. The general moment equation derived in Appendix A, is:

$$\frac{\partial M_n}{\partial t} - \frac{nK_1 M_B C_g}{\rho_t} M_{n-1} - K_f {}_B C_g r_f{}^n + \phi_i M_o M_n - \frac{1}{2}\phi_i \sum_{i=0}^{n}\binom{n}{i} M_i M_{n-i} = 0 \qquad 2.16$$

Expanding equation 2.16 for the first two moments yield

$$\frac{\partial M_o}{\partial t} - K_f \rho_{B_i} C_g + \frac{1}{2}\phi_i M_o{}^2 = 0 \qquad 2.17$$

$$\frac{\partial M_1}{\partial t} - \frac{K_1 M_B C_g}{\rho_t} - K_f \rho_{B_i} C_g r_f = 0 \qquad 2.18$$

These two moment equations are closed. They are related to the micropore surface area and volume by:

$$S_i = \frac{2sM_o}{\rho_{B_i}} \qquad 2.19$$

$$V_i = \frac{2sM_1}{\rho_{B_i}} \qquad 2.20$$

The micropore volume, V_i, and the micropore apparent density, are related by equation 2.15 and the micropore apparent density gives the micropore conversion by equation 2.14. Equations 2.14 and 2.15 were used

to convert volume data to micropore conversion. Using equations 2.14, 2.15, 2.19 and 2.20, equations 2.17 and 2.18 can be solved for in terms of their relative properties and local conversion.

$$\frac{d\Gamma_i}{dt} = \frac{\Gamma_i}{(1-x_i)}\left(\frac{dx_i}{dt}\right) + B_3 - B_4\Phi_i^*\Gamma_i^2(1-x_i) \qquad 2.21$$

$$\frac{dx_i}{dt} = (B_1\Gamma_i + B_2)(1-x_i) \qquad 2.22$$

where $\Gamma_i = \frac{S_i}{S_i^\circ}$, the relative micropore surface area and $\Phi_i^* = \phi_i/\phi_i^\circ$, the relative pore combination function. B_1 to B_4 are coefficients defined in Appendix A.

Hashimoto and Miura[3] had related it to the rate of pore growth (See equation 2.7, p. 10). However, they had to modify the pore growth rate function to obtain the combination function as a function of conversion. In this work, the relative pore combination function, Φ_i^*, was of the same form as Hashimoto and Miura's:

$$\Phi_i^* = \frac{1}{(1-x_i)^{n_i}} \qquad 2.23$$

The only parameters that were determined from the rate data were K_i, K_f, n_i and ϕ_i°. Equations 2.17 and 2.18 can be integrated to obtain the relative micropore surface area and conversion. They are independent from the macropore development, but the macropores are influenced by the micropore conversion due to the change in porosity.

The macropores were modeled in a similar manner to the original population balance model by Hashimoto and Silveston.[4,5] The macropores were assumed to be long cylindrical shaped pores with a radius greater than 100Å.

The density of the macropore wall will be the overall apparent density, $\rho_{B_{oa}}$, which is calculated by equation 2.13. By employing, $\rho_{B_{oa}}$, we take into account the presence of micropores and other macropores. Therefore, the rate of growth of a macropore will be:

$$\frac{dr_a}{dt} = \frac{K_a M_B C_g}{\rho_{B_{oa}}} \qquad 2.24$$

The introduction of a new pore of radius, r_c, by coalescence with adjacent pores is given by:

$$B_c = \frac{1}{2} \Phi a \int_0^r f(r_c) f(r_1) dr_1 \qquad 2.25$$

The radius of the pore due to the coalescence, r_c, can be found by assuming that the pore is cylindrical. This yields

$$r_c = \frac{2V}{S} = \frac{r_1^2 + r_2^2}{r_1 + r_2} \qquad 2.26$$

Hashimoto and Silveston[4,5] linearized the function to:

$$r_c = \alpha(r_1 + r_2) \qquad 2.27$$

where $\alpha = 0.5$ when $r_1 \equiv r_2$ and $\alpha = 1.0$ when $r_1 >> r_2$. In the pelletized material the macropore distribution was very narrow and would suggest $\alpha = 0.5$. However, the non-pelletized material had a very wide distribution, which would suggest that α be greater than 0.5.

The removal of pores due to combination is similar to equation 2.25. The loss is due to a pore of radius, r, combining with a pore of any other radii.

$$D = \phi_a f(r) \int_o^\infty f(r_1) dr_1 \qquad 2.28$$

The parameter, ϕ_a, in equation 2.25 and 2.28 was the pore combination probability function, which is to say that ϕ_a, defines the rate at which pores will combine, provided they are significantly close together.

Equations 2.24, 2.25, 2.27 and 2.28 were substituted into the general moment equation and expanded for the first three moments. This development is shown in Appendix A. The first three moments are:

$$\frac{dM_o}{dt} + \phi_a \left(1 - \frac{\alpha}{2}\right) M_o^2 = 0 \qquad 2.29$$

$$\frac{dM_1}{dt} - \frac{K_a M_B C_g}{\rho_{B_{oa}}} M_o + (1 - \alpha^2) \phi_a M_o M_1 = 0 \qquad 2.30$$

$$\frac{dM_2}{dt} - \frac{2K_a M_B C_g}{\rho_{B_{oa}}} M_1 + (1 - \alpha^3) \phi_a M_o M_2 - \alpha^3 \phi_a M_1^2 = 0 \qquad 2.31$$

By using the moment relations,

$$M_o = \frac{L_a \rho_{B_{oa}}}{\bar{\ell}} \qquad 2.32$$

$$M_1 = \frac{S_a \rho_{B_{oa}}}{2\pi\bar{\ell}} \qquad 2.33$$

$$M_2 = \frac{V_a \rho_{B_{oa}}}{\pi\bar{\ell}} \qquad 2.34$$

equations 2.29, 2.30 and 2.31 were solved in terms of the macropore length, surface area and volume.

$$\frac{d\Lambda_a}{dt} = \Lambda_a \left[B_5 \left(\frac{d\Omega_a}{dt}\right) + \frac{B_6}{(1-x_i)^2}\left(\frac{dx_i}{dt}\right)\right](1-x_{oa}) - \left(1-\frac{\alpha}{2}\right) \qquad 2.35$$

$$B_9 \Phi_a^* \Lambda_a (1-x_{oa})$$

$$\frac{d\Gamma_a}{dt} = \Gamma_a \left[B_5 \left(\frac{d\Omega_a}{dt}\right) + \frac{B_6}{(1-x_i)^2}\left(\frac{dx_i}{dt}\right)\right](1-x_{oa}) + \frac{B_8 \Lambda_a}{(1-x_{oa})} - \qquad 2.36$$

$$2\pi(1-\alpha^2)B_9 \Phi_a^* \Lambda_a \Gamma_a (1-x_{oa})$$

$$\frac{d\Omega_a}{dt} = \frac{\Omega_a}{(1-B_5(1-x_{oa})\Omega_a)}\left[\frac{B_6(1-x_{oa})}{(1-x_i)^2}\right]\left(\frac{dx_i}{dt}\right) + \frac{B_7 \Gamma_a}{B_5(1-x_{oa})(1-B_5(1-x_{oa})\Omega_a)} -$$

$$\frac{(1-\alpha^3)B_9 \Phi_a^* \Lambda_a \Omega_a (1-x_{oa})}{(1-B_5(1-x_{oa})\Omega a)} + \frac{\alpha^3 B_9 S_a^{o2} \Phi_a^* \Gamma^2 (1-x_{oa})}{4\pi L_a^o V_a^o (1-B_5(1-x_{oa})\Omega_a)} \qquad 2.37$$

The grouped parameters B_1 through B_9 are defined in Appendix A. Φ_a^* is the relative macropore combination probability and was assumed to be of the same general form as the micropore combination, equation 2.23.

$$\Phi_a^* = \frac{1}{(1-x_{oa})^{n_a}} \qquad 2.38$$

Therefore, only K_a, ϕ_a^o, n_a, and α had to be determined experimentally.

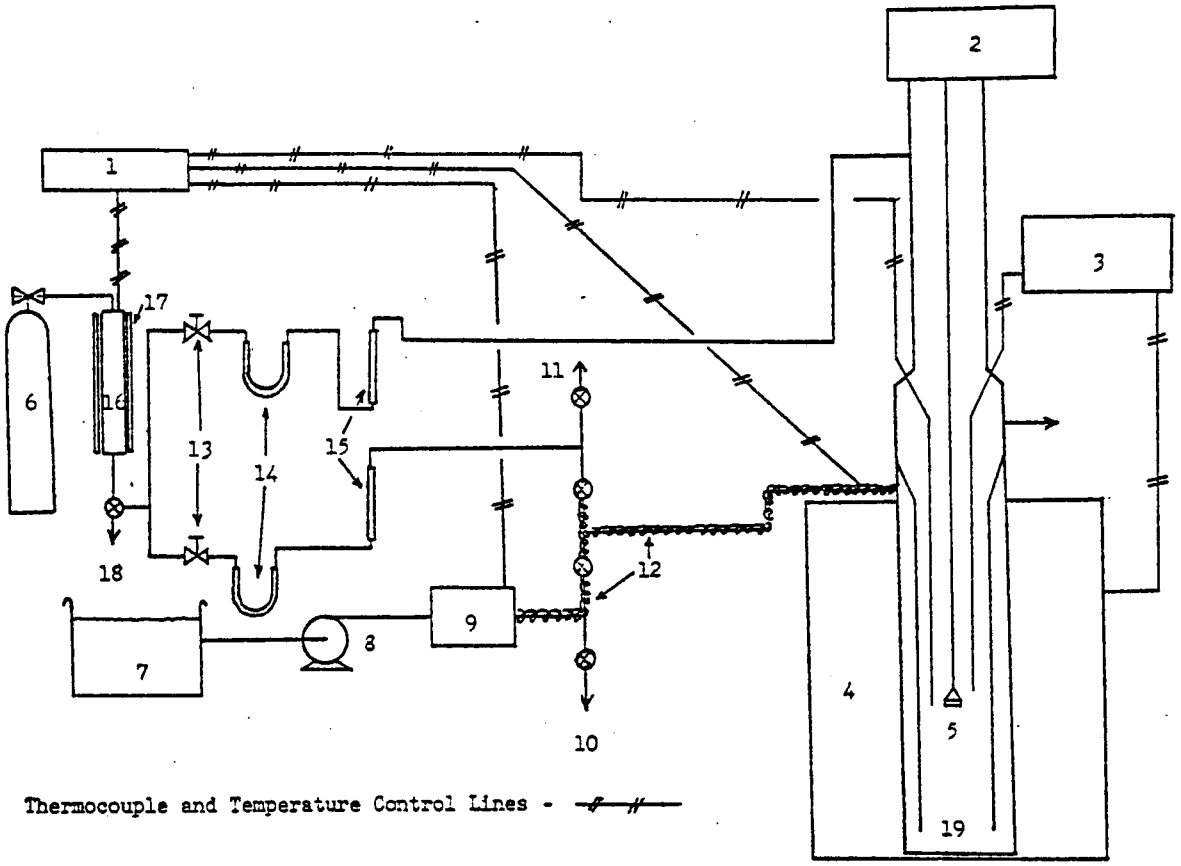
Equations 2.35, 2.36 and 2.37 for the macropores and equations 2.11 and 2.22 for the micropores could be integrated numerically to obtain the change in pore structure as a function of time.

CHAPTER III

EXPERIMENTAL

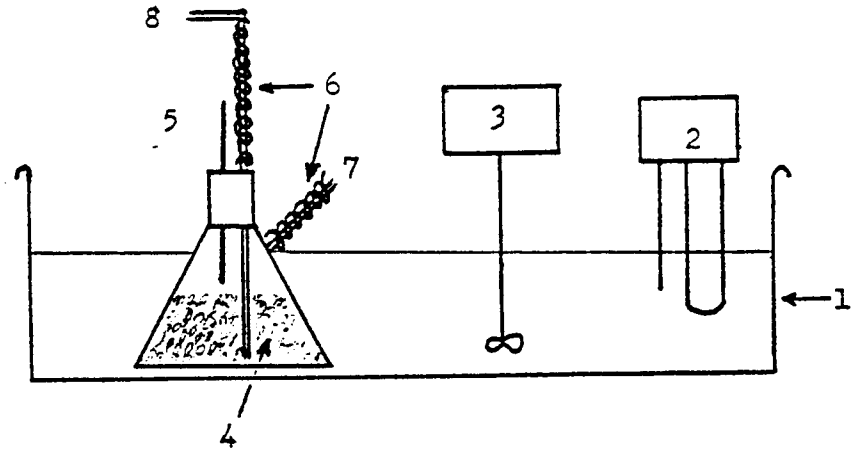
A. APPARATUS

The experimental apparatus used to obtain the kinetics data is shown in Figure 3.1. Three different steam systems were used to vary the steam partial pressure from 0.1 to 1.0 atmosphere. The low partial pressures (0.1 to 0.25 atm) were obtained by using a saturator (See Figure 3.2a); a similar system was used by Riede and Hanesian[11] for their study of the kinetics of the graphite-steam reaction. The nitrogen was saturated by bubbling it through a vacuum flask partially filled with 1/4 inch Raschig rings and distilled water. The temperature above the distilled water was measured and assumed to be the saturation temperature. The flask was placed in a constant temperature bath, which was heated by an immersion heater and controlled by a thermoswitch. Partial pressures between 0.25 and 1.00 atm were obtained by mixing streams of pure steam and nitrogen in the apparatus shown in Figure 3.2b. The two streams were fed into a spherical manifold (volume 33.5 cm^3) with sufficient hold up time (4.0 sec at 500 cc/min) to allow good mixing. Further mixing also occurs in the annulus of the reactor. For 100 percent steam, the system in Figure 3.1 and Figure 3.2b was employed. A micro-metering pump was used to feed distilled water to the steam generator. The micro-balance was made by the Shinko Denshi Co., Ltd. It was connected to an amplifier which lead to a continuous recorder. The overall sensitivity was about 0.5 mg. The furnace was an electrical resistance type with a maximum temperature of 1200°C. The temperature in the reactor was controlled by



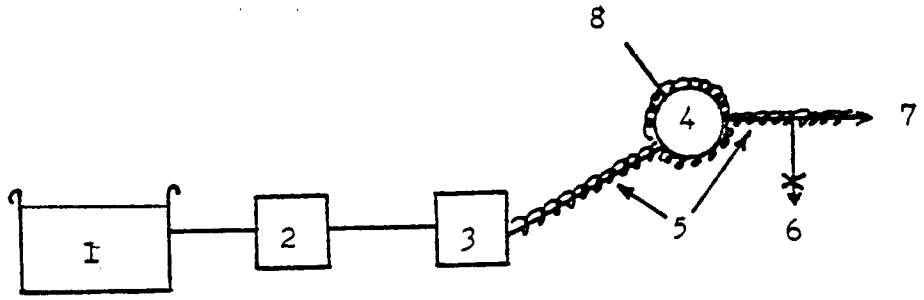
1. Temperature Recorder
2. Micro-balance
3. Temperature Controller
4. Furnace
5. Platinum Basket
6. Nitrogen Supply
7. Distilled Water Supply
8. Micro-pump
9. Steam Generator
10. Steam Vent
11. Nitrogen Vent
12. Heating Tape
13. Control Valves
14. Drying Columns (Silca Gel)
15. Rotameters
16. Copper Deoxygen
17. Heating Jacket
18. Three-way Valve
19. Quartz Reactor

Figure 3.1. Experimental Apparatus.



1. Constant Temperature Bath
2. Immersion Heater and Thermoswitch
3. Agitator
4. ¼" Raschig Rings and Distilled Water
5. Thermometer
6. Heating Tape
7. Outlet to the Reactor
8. Nitrogen Inlet

(a)



1. Distilled Water
2. Micro-pump
3. Steam Generator
4. Mixing Manifold
5. Heating Tape
6. Vent
7. Outlet to the Reactor
8. Nitrogen Inlet

(b)

Figure 3.2. Low Partial Pressure Steam Apparatus.
(a) For $P_{H_2O} < 0.25$ atm.
(b) for $P_{H_2O} \geq 0.25$ atm.

a solid state PID controller. The temperature sensors were Chomel-Alumel thermocouples located inside the reactor. The reactor was made of quartz glass. Dimensions and specifications on the equipment are listed in Appendix B.

B. SAMPLE MATERIALS

Two different preparations of coal char were employed in the steam activation experiments. One was a pelletized material (Miike Coal) and the other was a non-pelletized material (Victoria Coal).

The pelletized material was prepared by the Miike Company. The starting coal char was ground to 1μ size and kneaded with a binder made from paper pulp waste. This mixture was charred at approximately 900°C. The ash and carbon contents are listed in Table 3.1.

The non-pelletized material was prepared from Victoria Coal. It was charred at approximately 900°C. The ash and carbon contents are listed in Table 3.1.

The ash and carbon contents listed in Table 3.1 are on a moisture and volatile matter free basis. The higher ash content for the pelletized material is probably due to the use of pulp waste as the binder. Also, due to the great differences in the ash contents all the other properties are based on an ash free or mineral matter free basis.

TABLE 3.1

COMPOSITION OF COAL CHAR

Coal Char	Percent Carbon	Percent Ash
Pelletized Coal	86.18	13.82
Non-Pelletized Coal	97.21	2.79

C. PROCEDURE

For a typical run, the reactor was opened and the sample basket removed. The deoxygen column heating unit was turned on, and while it was heating the sample was prepared. The sample basket was heated over a Bunsen burner for about one minute to remove traces of unburned carbon and moisture. Then it was weighed and the sample added and reweighed. The sample weight was determined as the difference between the two. The sample and basket were then placed inside the reactor. The ground glass joints between the upper and lower parts of the reactor were sealed with vacuum grease and the whole assembly was closed. The micro-balance and recorders were turned on and their proper scale ranges were selected. The micro-balance was zeroed. The inlet stop cocks on the nitrogen and steamline were closed and the vents opened. All heating tapes and the steam generator were turned on. If the saturator was used, the water bath heater was turned on an hour prior to the start of the test. The micropump, which feeds water to the steam generator, was not turned on until the steam generator's internal temperature was greater than 100 °C. The nitrogen inlet stop cock was opened and the vent closed. The basket was checked to see if it was still floating freely.

The gasification temperature was selected on the temperature controller, and it was turned on. It took about 45 minutes to an hour for the reactor to reach the desired temperature. If a temperature lower than 850 °C was used the system was heated to 900 °C, and when a constant weight was achieved it was cooled down to the proper temperature. Once a constant weight was achieved the gasification could begin. All lines that were to touch steam were checked to see if they were above 100 °C, and the micropump was checked to see if it was set at the proper flow rate. The steam was valved in as follows: (1) the nitrogen vent was opened, (2) the steam inlet stop cock was opened, (3) the nitrogen inlet stop cock was closed, and (4) the steam vent was closed. This sequence took about 10 to 15 seconds to complete and so the mixing of the steam and the nitrogen was small and would have little affect on the gasification rate. Usually a small deflection was noticed on the strip chart that recorded the weight, due to the valving in sequence. There was a delay of about 45 seconds before the recorder would indicate the start of gasification because of the length of tubing and the volume in the reactor that had to be displaced by the steam. The first deflection after the valving in deflection was taken as the starting point.

The test was usually continued for 1 to 1 1/2 hours. At the end of the test air was let in through the nitrogen lines by way of a three-way valve. The steam was shut off, and the air was allowed to react with the sample unitl no more carbon remained. During the experiment, the weight loss was continually recorded and the temperature of the reactor, steam generator, inlet line, steamline and the deoxygen column were recorded. The system was shut down; the furnace was opened and allowed to cool. Once the system was cool, the sample bucket was removed and the ash

remaining was determined. The carbon content of the sample was calculated as the difference between the flat line obtained at the beginning of gasification and the flat line obtained after the sample was burned with air (See Figure 3.3).

D. SYSTEM CHARACTERIZATION AND PRELIMINARY TESTS

A series of experiments were run to determine the effect of sample size, particle radius, steam flow rates and temperature stability. These were run to find the conditions under which the reaction was kinetically controlled and isothermal.

Four different particle diameters were tested (0.546 mm, 0.650 mm, 1.076 mm, and 2.20 mm) using the pelletized coal char. All of the runs with the three smaller diameters and a sample weight of approximately 45 mg were within the two standard deviation limits (See Table 3.2, Run 4b 4e, 6c, and 8a). However, the largest diameter (2.20mm) showed a much slower rate and was outside the limit (See Table 3.2, Run 9a). This indicated that diffusional resistances are beginning to have an effect at this particle size. This is also demonstrated by the calculation of an effectiveness factor for the micropores (See Appendix C). If the smallest of the particles is assumed to have an effectiveness factor close to one (0.98 - 0.99), then the next to the largest particle (D = 1.076 mm) has a factor of 0.92 to 0.96. However, the largest particle has an effectiveness factor of only 0.75 to 0.86. This shows that the smaller particles were in the region where the reaction was kinetically controlled and diffusional resistances in the micropores were only beginning to affect the largest particles. The remainder of the tests were run with the 0.65 mm and 1.076 mm diameter particles.

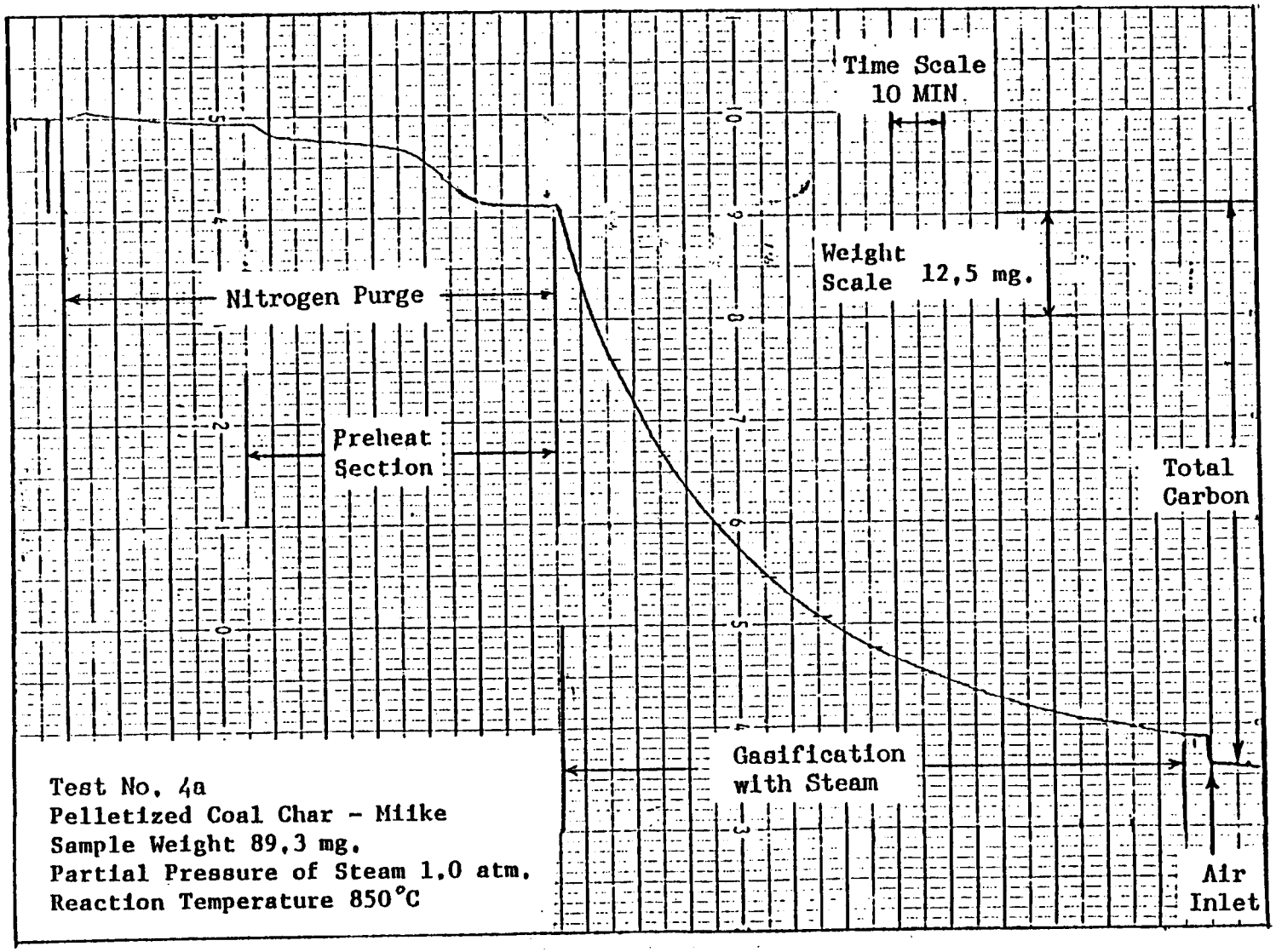


Figure 3.3. Gasification Experiment on the Micro-Balance Apparatus.

TABLE 3.2

SYSTEM CHARACTERIZATION EXPERIMENTS FOR THE MICRO-BALANCE USING OVERALL CONVERSION DATA FOR PELLETIZED COAL CHAR**

Reaction Time(Min)	Overall Conversion												
	4a	4b	4c	4d	4e	4f	5a	6a	6b	6c	8a	9a	Average*
5				0.1899	0.1456	0.1537		0.1708	0.1474	0.1708	0.1802	0.0689	0.1655
10	0.2725	0.2819	0.2450	0.3297	0.2606	0.2748	0.2634	0.3017	0.2674	0.2858	0.2808	0.1626	0.2785
15					0.3570	0.3696		0.3959	0.3633	0.3788	0.3965	0.2450	0.3769
20	0.4452	0.4544	0.4240	0.5405	0.4390	0.4441	0.4241	0.4669	0.4521	0.4580	0.4559	0.3267	0.4549
25					0.5072	0.5512				0.5289	0.5384	0.4020	0.5314
30	0.5677	0.5811	0.5591	0.6628	0.5629	0.6056	0.5536	0.5703	0.5825	0.5888	0.5897	0.4638	0.5840
35						0.6537							
40	0.6632	0.6831	0.6579	0.7432	0.6594	0.7034	0.6519	0.6343	0.6816	0.6839	0.6744	0.5717	0.6760
45						0.7453							
50	0.7313	0.7572	0.7345	0.7899	0.7275	0.7981	0.7277	0.6721	0.7468	0.7507	0.7424	0.6584	0.7435
55						0.8214							
60	0.7904	0.8135	0.7825	0.8486	0.7875	0.8556	0.7813	0.7302	0.7808	0.8023	0.7974	0.7273	0.7913
70	0.8313	0.8592	0.8333	0.8574	0.8364	0.9006	0.8259	0.7994	0.8323	0.8402	0.8365	0.7777	0.8411
80	0.8676	0.8910	0.8626	0.9162	0.8674		0.8661	0.8285	0.8767	0.8747	0.8712	0.8260	0.8722
90	0.8948	0.9225	0.8918	0.9209	0.8942		0.8973	0.8698	0.9112	0.8988	0.8951	0.8643	0.8996
100	0.9176	0.9437	0.9175				0.9151	0.9012	0.9386		0.9117		0.9208
110	0.9311	0.9507	0.9357				0.9286						0.9365
120	0.9448	0.9544	0.9468				0.9464						0.9481

*The average excludes run 9a because it lies outside the error limit of two standard deviations, $\sigma = \sqrt{\frac{\Sigma (\bar{x} - x_i)}{n}} = 0.0245$

** The experimental conditions are given in Table 3.4, p. 30.

A similar series of tests were run to determine what steam flow rate to run to reduce the effects of external mass transfer to the particle. At a reactor temperature of 800°C and a partial pressure of steam of 1.0 atm. flow rates of 200 cc/min, 400 cc/min and 500 cc/min of STP steam were run. The run at 200 cc/min STP steam showed a slightly lower reaction rate (See Table 3.3, Run 2a). There was no significant difference between the 400 cc/min and 500 cc/min data (See Table 3.3, Run 1a and 3a). Also, at 850°C and a partial pressure of steam of 1.0 atm., flow rates of 500 cc/min and 591 cc/min STP of steam were run. There was no significant difference in their rates (See Table 3.2, Run 5a, p. 27). It was concluded from these tests that any flow rate greater than or equal to 400 cc/min STP was sufficient to reduce the effects of external mass transfer. Therefore, the remaining runs were run at 500 cc/min STP overall flow rate.

The sample weight was also varied to determine if the depth of sample in the bucket or the sensitivity of the micro-balance would effect the reaction rate. Sample weights of 20 mg, 45 mg, 90 mg and 200 mg were run. The 20 mg, 45 mg and 90 mg samples were only one layer thick and so the depth of the sample was not a problem. A 20 mg sample was used in 4 runs (See Table 3.2, Runs 4c, 4d, 6a, and 6b, p. 27) and they showed a wider scatter at high conversion than the larger sample weights. This was due to the sensitivity of the micro-balance, which was ± 0.5 mg. The sensitivity becomes significant at high conversion because of the very small sample weight that remains. The remaining tests were run with sample weights between 45 mg and 90 mg.

TABLE 3.3

MICRO-BALANCE OVERALL CONVERSION DATA FOR PELLETIZED COAL*

Reaction Time(Min)	Overall Conversion						
	1a	2a	2b	3a	3b	3c	VP-1a
5			0.0478		0.0387	0.0072	0.0303
10	0.1672	0.1272	0.0888	0.1601	0.0843	0.0359	0.0729
15			0.1287		0.1271	0.0598	0.1132
20	0.2740	0.2225	0.1777	0.2597	0.1547	0.0813	0.1547
25			0.2141		0.1823	0.1017	0.1951
30	0.3483	0.2907	0.2494	0.3289	0.1989	0.1232	0.2332
35			0.2802			0.1411	0.2691
40	0.4040	0.3497	0.3064	0.3939	0.2334	0.1555	0.3061
45			0.3462			0.1746	0.3397
50	0.4551	0.3997	0.3702	0.4415	0.2652	0.1890	0.3733
55			0.3941			0.2225	0.4036
60	0.5061	0.4406	0.4203	0.4804	0.3011	0.2416	0.4339
70	0.5480	0.4816		0.5194	0.3412	0.2967	0.4910
80	0.5804	0.5178		0.5583	0.3508		0.5404
90	0.6129	0.5541		0.5930	0.3881		0.5841
100	0.6455	0.5859		0.6189	0.4047		0.6267
110	0.6733	0.6132		0.6406	0.4213		0.6648
120	0.6966	0.6359		0.6622	0.4420		0.7018

Reaction Time(Min)	Overall Conversion		
	VP-2a	VP-3a	VP-4a
1.5	0.0220	0.0193	0.0014
3.0	0.0565	0.0411	0.0096
4.5	0.0895	0.0628	0.0220
6.0	0.1226	0.0882	0.0343
7.5	0.1529	0.1099	0.0467
9.0	0.1832	0.1304	0.0604
10.5	0.2163	0.1546	0.0755
12.0	0.2438	0.1751	0.0893
13.5	0.2700	0.1957	0.1003
15.0	0.2948	0.2138	0.1099
18.0	0.3457	0.2524	0.1366
21.0	0.3884	0.2886	0.1538
24.0	0.4311	0.3200	0.1754
27.0	0.4711	0.3575	0.1951
30.0	0.5000	0.3889	0.2157
33.0	0.5331	0.4215	0.2335
36.0	0.5634	0.4517	0.2527
39.0	0.5895	0.4795	0.2706
42.0	0.6185	0.5060	0.2871
45.0	0.6460	0.5326	0.3022

*The experimental conditions are given in Table 3.4.

TABLE 3.4

EXPERIMENTAL CONDITIONS FOR MICRO-BALANCE EXPERIMENTS WITH PELLETIZED COAL CHAR

Experimental Run Number	Sample Weight (mg)	Mesh Size (Tyler)	Particle Diameter (mm)	Gas Flow Rate (cc/min) STP	Partial Pressure of Steam (atm)	Reactor Temperature (°C)	Total Pressure (mm.Hg)	Preheat Temperature (°C)
1a	89.0	-14+16	1.076	400	1.0	800	759.4	-
2a	89.1	-14+16	1.076	200	1.0	800	753.5	-
2b	58.2	-14+16	1.076	500	1.0	800	762.8	900
3a	91.3	-14+16	1.076	500	1.0	800	761.3	-
3b	44.6	-14+16	1.076	500	1.0	750	759.5	-
3c	55.3	-14+16	1.076	500	1.0	750	763.1	850
4a	89.3	-14+16	1.076	500	1.0	850	762.6	-
4b	45.3	-14+16	1.076	500	1.0	850	762.6	-
4c	20.2	-14+16	1.076	500	1.0	850	760.5	-
4d	20.6	-14+16	1.076	500	1.0	850	760.5	-
4e	47.5	-14+16	1.076	500	1.0	850	760.0	-
4f	204.4	-14+16	1.076	500	1.0	850	755.4	-
5a	89.0	-14+16	1.076	500	1.0	850	760.0	-
6a	20.2	-24+28	0.650	500	1.0	850	758.2	-
6b	20.1	-24+28	0.650	500	1.0	850	758.9	-
6c	45.1	-24+28	0.650	500	1.0	850	760.0	-
8a	44.1	-28+32	0.546	500	1.0	850	757.9	-
9a	46.3	- 8+ 9	2.000	500	1.0	850	760.0	-
VP-1a	57.6	-14+16	1.076	500*	0.103	850	760.0	-
VP-2a	50.2	-14+16	1.076	500**	0.50	850	756.0	900
VP-3a	53.3	-14+16	1.076	600**	0.25	850	758.5	900
VP-4a	55.2	-14+16	1.076	500**	0.50	850	755.2	900

*This was the flow rate of H_2, the saturator temperature was 46.5°C.

**This was the total flow rate, H_2 plus steam.

Another test was performed to see if the endothermic reaction between the steam and the carbon would significantly reduce the temperature inside the bucket. The reactor temperature thermocouple was placed so the tip was embedded in the sample. The largest decrease in temperature was seen immediately after the sample started reacting and was only 4°C and decreased as the reaction continued. This was at the highest reaction rate conditions, 850°C and partial pressure of steam of 1.0 atm. It was therefore assumed that the temperature gradient was small and the reactor temperature was assumed to be the reaction temperature.

These experiments were used to characterize the reactor system. It was determined that at conditions where flow rates were greater than or equal to 400 cc/min STP gas, particle sizes between 0.546 mm and 1.076 mm, and sample sizes between 20.0 mg and 200 mg were sufficient to assure that the reaction was kinetically controlled and the particle could be assumed to be isothermal during the course of the reaction.

A pair of experiments were run to show that the pore structure development was the same for the micro-balance as in the fluidized bed. The pelletized material was reacted for 9.0 minutes and the non-pelletized material for 6.0 minutes. The surface areas were measured by the BET method using nitrogen adsorption at 77.5°K. The macropore volumes were determined by mercury penetration. The pelletized material agreed well with the fluidized bed data (See Table 3.5). The non-pelletized material had a much smaller macropore volume from the micro-balance data (See Table 3.5). However, at this low conversion some of the macropore volume was still in void which were inaccessible to the mercury penetration and this can also account for the slightly lower BET surface area. The data was sufficiently close, and it was assumed that the pore structures were developing in a similar manner.

TABLE 3.5

PORE DEVELOPMENT COMPARISON BETWEEN THE MICRO-BALANCE AND THE FLUIDIZED BED

	x_f	Macropore Volume cc/gm	Surface Area m^2/gm
Pelletized			
Micro-balance	0.25	0.315	331
Fluidized Bed	0.25	0.323	413
Non-Pelletized			
Micro-balance	0.1607	0.0685	606
Fluidized Bed	0.1607	0.1938	675

CHAPTER IV

RESULTS AND DISCUSSION

A. SUMMARY OF DATA FROM THE MICRO-BALANCE

The rate data from the micro-balance for the pelletized material are summarized in Tables 3.2, 3.3, and 3.4, pp. 27-30 and Tables 4.1 and 4.2 for the non-pelletized material. Both the pelletized and the non-pelletized material were run at various partial pressures and temperatures. At 850 °C, four partial pressures, 1.0, 0.5, 0.25 and 0.103 atmospheres were employed to determine the proper form of the rate equation. Three different temperatures, 850°C, 800°C and 750°C were run at 1.0 atmosphere partial pressure of steam to determine the activation energies of the different rate constants. The partial pressure of steam was also varied at 800°C. The pelletized coal char was run at 1.0 and 0.5 atmospheres and the non-pelletized coal char at 1.0 and 0.25 atmospheres. These data were combined with the data by Imai[5] and Yoshikawa[20]. They had obtained pore structure data on the same coal chars using a small fluidized bed reactor (See Table 4.3 and 4.4). This gave the properties as a function of time, provided that at a given conversion the property development was the same in both the micro-balance reactor and the bench scale fluidized bed. This was shown to be true in Table 3.5, p. 32. This would also be the case, if the reaction rates in both systems were kinetically controlled. The only other difference would be the external burn-off of the particle, which would be higher in the fluidized bed because of the abrasive action of the particles in the bed.

TABLE 4.1

MICRO-BALANCE OVERALL CONVERSION DATA FOR NON-PELLETIZED COAL CHAR*

Reaction Time(Min)	Overall Conversion							Reaction Time(Min)	Overall Conversion				
	21b	22a	23a	23b	VP-21a	VP-22a	VP-23a		21c	VP-22b	VP-23b	VP-24a	VP-25a
5	0.1330	0.0792	0.0266	0.0088	0.0445	0.1119	0.1178	1.5	0.0433	0.0390	0.0288		
10	0.2659	0.1557	0.0519	0.0290	0.0954	0.2393	0.2277	3.0	0.0789	0.0753	0.0551	0.0239	0.0220
15	0.3670	0.2199	0.0771	0.0467	0.1438	0.3429	0.3285	4.5	0.1247	0.1182	0.0911		
20	0.4765	0.2760	0.1024	0.0644	0.2010	0.4452	0.4045	6.0	0.1692	0.1610	0.1163	0.0465	0.0495
25	0.5734	0.3374	0.1210	0.0808	0.2519	0.5333	0.4738	7.5	0.2201	0.2000	0.1451		
30	0.6551	0.3852	0.1449	0.0997	0.2964	0.6143	0.5419	9.0	0.2646	0.2377	0.1715	0.0766	0.0714
35	0.7175			0.1187	0.3410		0.6034	10.5		0.2753	0.1978		
40	0.7729	0.4863	0.2101	0.1351	0.3855		0.6544	12.0	0.3435	0.3143	0.2230	0.0992	0.0962
45	0.8199			0.1528	0.4262		0.7042	13.5		0.3468	0.2458		
50	0.8546	0.5833	0.2473	0.1705	0.4606		0.7474	15.0	0.4186	0.3792	0.2722	0.1269	0.1223
55	0.8809			0.1843	0.5000		0.7827	18.0	0.4796	0.4390	0.3213	0.1559	0.1456
60	0.9072		0.3178	0.1970	0.5280		0.8141	21.0	0.5407	0.4987	0.3645	0.1834	0.1690
70	0.9391	0.7445	0.3524	0.2235				24.0	0.5954	0.5571	0.4089	0.2048	0.1923
80	0.9598	0.7855	0.3843					27.0	0.6438	0.6078	0.4496	0.2274	0.2198
90	0.9765	0.8224	0.4229					30.0	0.6807	0.6429	0.4904		0.2404
100		0.8634						33.0	0.7201		0.5264		0.2637
110		0.8975						36.0	0.7519		0.5635		0.2843
120		0.9153						39.0	0.7786		0.5959		0.3049
								42.0	0.8066		0.6283		0.3283
								45.0	0.8333		0.6571		0.3516
								48.0			0.6823		0.3750
								54.0			0.7302		0.4052
								60.0			0.7674		0.4451

*The experiment conditions are given in Table 4.2.

TABLE 4.2

EXPERIMENTAL CONDITIONS FOR MICRO-BALANCE EXPERIMENTS WITH NON-PELLETIZED COAL CHAR

Experimental Run Number	Sample Weight (mg)	Mesh Size (Tyler)	Particle Diameter (mm)	Gas Flow Rate (cc/min) STP	Partial Pressure of Steam (atm)	Reactor Temperature (°C)	Total Pressure (mm.Hg)	Preheat Temperature (°C)
21b	45.1	-14+16	1.076	500	1.0	850	753.4	-
22a	45.5	-14+16	1.076	500	1.0	800	759.5	-
23a	45.4	-14+16	1.076	500	1.0	750	754.9	-
23b	51.3	-14+16	1.076	500	1.0	750	761.9	900
VP-21a	52.6	-14+16	1.076	500*	0.103	850	763.7	-
VP-22a	56.1	-14+16	1.076	500**	0.50	850	760.8	900
VP-23a	52.4	-14+16	1.076	550**	0.273	850	760.8	900
21c	52.9	-14+16	1.076	500	1.0	850	750.7	900
VP-22b	51.9	-14+16	1.076	500**	0.50	850	-	900
VP-23b	54.0	-14+16	1.076	600**	0.25	850	763.5	-
VP-24a	51.7	-14+16	1.076	500**	0.5	800	769.7	900
VP-25a	50.1	-14+16	1.076	600**	0.25	800	763.5	900

*This was the flow rate of N_2, the saturator temperature was 46.75 °C.

**This was the total flow rate, N_2 plus steam.

TABLE 4.3

PORE STRUCTURE DATA FOR PELLETIZED COAL CHAR

Experimentor	x_f	x_c	x_{oa}	x_i	V_i cm^3/gm	S_i m^2/gm	V_a cm^3/gm	Ω_a	Γ_a **	Λ_a **	R'_a	R'_{ex}	Temperature (°C)	Pressure (atm)
Yoshikawa	0.0000	0.0000	0.000	0.000	0.174	520	0.120	1.000	1.00	1.000	1.00	1.000	850	1.0
	0.0818	0.0799	0.089	0.028	0.195	357.7	0.181	1.508	1.44	1.368	1.05*	1.003	850	1.0
	0.156	0.1346	0.139	0.028	0.195	650.6	0.235	1.958	1.632	1.360	1.20*	0.9934	850	1.0
	0.245	0.2228	0.242	0.070	0.228	906.0	0.335	2.792	1.86	1.240	1.50	0.9974	850	1.0
	0.441	0.3936	0.416	0.215	0.371	1232.5	0.521	4.342	2.00	0.926	2.16	0.9630	850	1.0
	0.594	0.5224	0.536	0.354	0.569	1268.9	0.697	5.808	2.11	0.768	2.75*	0.9444	850	1.0
	0.669	0.5959	0.6066	0.379	0.613	1526.9	0.945	7.875	2.36	0.709	3.33	0.9274	850	1.0
	0.808	0.7188	0.702	0.489	0.864	1478.9	1.414	11.783	2.81	0.668	4.20*	0.8497	850	1.0
	0.908	0.8088	0.802	0.577	1.157	1517.1	2.542	21.183	4.24	0.848	5.00	0.7732	850	1.0
Imai	0.189	0.1694	0.197	0.030	0.196	827.9	0.304	2.533	1.809	1.29	1.40*	0.9959	850	1.0
	0.384	0.1694	0.376	0.173	0.325	1201.3	0.475	3.958	1.931	0.942	2.05*	0.9812	850	1.0
	0.541	0.4838	0.497	0.286	0.463	1441.3	0.662	3.517	2.098	0.798	2.63*	0.9593	850	1.0
	0.648	0.5818	0.589	0.366	0.591	1588.6	0.905	7.542	2.320	0.714	3.25*	0.9362	850	1.0
	0.742	0.6675	0.662	0.440	0.742	1564.1	1.198	9.983	2.590	0.674	3.85*	o.8941	850	1.0
	0.1648	0.1467	0.1649		0.169		0.291	2.425				1.000	800	1.0
	0.3297	0.2934	0.3316	0.1685	0.320	1089.0	0.391	3.258				1.000	800	1.0
	0.4612	0.4105	0.4505	0.2568	0.423	1155.0	0.560	4.667				0.9935	800	1.0
	0.5773	0.5138	0.5215	0.3393	0.544	1325.0	0.666	5.55				0.9595	800	1.0
	0.6933	0.6170	0.5905	0.4154	0.686	1646.0	0.820	6.83				0.9081	800	1.0
	0.2000	0.1779	0.1591		0.162	439.0	0.291	2.425				0.9835	900	1.0
	0.2657	0.2365	0.2669	0.10	0.254		0.346	2.883				1.000	900	1.0
	0.3522	0.3135	0.3219	0.124	0.276	654.0	0.417	3.475				0.9849	900	1.0
	0.5290	0.4708	0.4833	0.2762	0.449	1300.0	0.631	5.258				0.9696	900	1.0
	0.6172	0.5493	0.5671	0.3417	0.548	1420.0	0.847	7.058				0.9598	900	1.0
	0.6830	0.6079	0.6121	0.3928	0.640	1664.0	0.980	8.170				0.9349	900	1.0

*Data taken from curve of the other pore radius by Yoshikawa, the initial macropore radius was 1200Å.

**The relative pore length and surface area were calculated by using the relationship for a cylindrical shape pore, S = 2V/R.

TABLE 4.4

PORE STRUCTURE DATA FOR NON-PELLETIZED COAL CHAR

Experimentor	x_f	x_c	x_{oa}	x_i	V_i cm^3/gm	S_i m^2/gm	V_a cm^3/gm	Ω_a	Γ_a*	Λ_a*	R'_{ex}	Temperature (°C)	Partial Pressure (atm)
Yoshikawa	0.000	0.000	0.000	0.000	0.1553	777.0	0.155	1.0	1.0	1.0		850	1.0
	0.090	0.087	0.090	0.149	0.282	1512.0	0.193	1.245	1.17	1.099	1.001	850	1.0
	0.136	0.135	0.120	0.170	0.304	1623.0	0.188	1.213	1.17	1.136	0.9942	850	1.0
	0.311	0.306	0.295	0.259	0.408	1847.0	0.388	1.987	1.68	1.418	0.9948	850	1.0
	0.580	0.571	0.473	0.4297	0.701	2257.0	0.486	3.135	2.44	1.898	0.9337	850	1.0
	0.773	0.751	0.646	0.5133	0.919	2274.0	0.910	5.871	4.07	2.825	0.8893	850	1.0
	0.879	0.856	0.762	0.5888	1.919	2117.0	2.099	13.542	7.54	4.202	0.8458	850	1.0

*Relative macropore surface area, Γ_a, and length, Λ_a, were not measured. It was assumed that the total micropore length per unit volume was constant, which would occur if coalescance is small. Therefore, $\Lambda_a = 1/(1-x_{oa})$, and since a cylindrical shape was assumed $\Gamma_a = \sqrt{\Omega_a \Lambda_a}$. The initial surface area was calculated by assuming a mean radius of 1033Å.

B. SUMMARY OF EQUATIONS AND DETERMINATION OF PARAMETERS

In Chapter II, five equations were developed to describe the gasification rate and pore structure development. There were two for the micropores and three for the macropores. The micropore conversion from equation 2.22 and the relative macropore volume from equation 2.37 were used in equations 2.13, 2.14 and 2.15 to give the overall internal conversion, x_{oa}. The overall conversion, x_f, was obtained by combining the internal conversion, x_{oa}, with the particle shrinkage:

$$x_f = 1 - (1 - x_{oa})\xi^3 \qquad 4.1$$

where ξ, is the relative particle radius. It was assumed that the external burn-off would occur by the same mechanism as the macropores. Therefore, for a spherical particle the rate of particle shrinkage becomes:

$$\frac{d\xi}{dt} = \frac{K_a M_B C_g^{\frac{1}{2}}}{R^o \rho_{B_{oa}}} \qquad 4.2$$

The rate expression was changed from first order to half order because of the experimental data. This was developed by examining the Langmuir type rate expression for low hydrogen concentration (equation 2.3).

$$\text{RATE} = \frac{K_1 P_{H_2O}}{1 + K_2 P_{H_2O}} \qquad 2.3$$

This will be between zero and first order depending upon the magnitude of $K_2 P_{H_2O}$. Hashimoto and Miura[3], Imai[6] and Yoshikawa[20] had assumed the reaction to be first order. Riede and Hanesian[11] obtained first order kinetics for the graphite-steam reaction over a temperature range of

500°C to 900°C and a total pressure of one atmosphere. However, the partial pressure of steam was low (0.09 to 0.158 atm.) and equation 2.3 becomes first order for low values $K_2P_{H_2O}$. The experimental conditions used in this work were the same except the partial pressure of steam was much higher (0.1 atm. to 1.0 atm.). Therefore, the rate equation was between zero and first order and was approximated by:

$$\text{RATE} = \frac{K_1P_{H_2O}}{1 + K_2P_{H_2O}} \approx K_1C_g^{\frac{1}{2}} \qquad 4.3$$

This did not affect the equations derived in Appendix A, which had assumed a first order reaction. The only change necessary was the replacement of KC_g with $KC_g^{\frac{1}{2}}$.

The rate of particle shrinkage, equation 4.2, was also modified because it assumed that the reactive surface is the surface of rigid spheres. This greatly underestimated the actual rate and so equation 4.2 was modified to give:

$$\frac{d\xi}{dt} = \frac{FK_aM_BC_g^{\frac{1}{2}}}{R_p\rho^o_{B_{oa}}(1-x_{oa})} \qquad 4.4$$

where F is an external surface area connection factor, which accounted for the underestimation of the external surface area due to the rigid sphere assumption and external loss due to effects other than gasification.

The overall reaction of the particle was given by six differential equations and two auxiliary equations. The micropores has two differential equations, one for conversion and one for the surface.

$$\frac{d\Gamma_i}{dt} = \frac{\Gamma_i}{(1-x_i)}\left(\frac{dx_i}{dt}\right) + B_3 - B_4\Phi_i^*\Gamma_i^2(1-x_i) \qquad 2.21$$

$$\frac{dx_i}{dt} = (B_1\Gamma_i + B_2)(1-x_i) \qquad 2.22$$

where $B_1 = K_i C_g^{\frac{1}{2}} M_B S_i^o$,

$B_2 = 2.0 r_f s_i \rho_t K_f C_g^{\frac{1}{2}}$

$B_3 = 2.0 s_i K_f C_g^{\frac{1}{2}}/S_i^o$,

$B_4 = \rho_{B_i}^o S_i^o \phi_i^o/4.0 s_i$,

$\Phi_i^* = \phi_i/\phi_i^o = 1/(1-x_i)^{n_i}$,

and the initial combination rate function, ϕ_i^o, was assumed to be related to the initial conversion rate. This yields

$$\phi_i^o \propto B_1 + B_2 \qquad 4.5$$

which becomes

$$\phi_i^o = \epsilon_i B_2 \qquad 4.6$$

Where ϵ_i is the proportionality constant, and it will be shown later that $B_1 << B_2$.

The macropores have three differential equations, one for the length, one for the surface area and another for the volume.

$$\frac{d\Lambda_a}{dt} = \Lambda_a\left[B_5\left(\frac{d\Omega_a}{dt}\right) + \frac{B_6}{(1-x_i)^2}\left(\frac{dx_i}{dt}\right)\right](1-x_{oa}) - \left(1-\frac{\alpha}{2}\right) \qquad 2.35$$
$$B_9\Phi_a^*\Lambda_a(1-x_{oa})$$

$$\frac{d\Gamma_a}{dt} = \Gamma_a\left[B_5\left(\frac{d\Omega_a}{dt}\right) + \frac{B_6}{(1-x_i)^2}\left(\frac{dx_i}{dt}\right)\right](1-x_{oa}) + \frac{B_8\Lambda_a}{(1-x_{oa})} - \qquad 2.36$$
$$2\pi(1-\alpha^2)B_9\Phi_a^*\Lambda_a\Gamma_a(1-x_{oa})$$

$$\frac{d\Omega_a}{dt} = \frac{\Omega_a}{(1-B_5(1-x_{oa})\Omega_a)}\left[\frac{B_6(1-x_{oa})}{(1-x_i)^2}\right]\left(\frac{dx_i}{dt}\right) + \frac{B_7\,\Gamma_a}{B_5(1-x_{oa})(1-B_5(1-x_{oa})\Omega_a)} -$$

$$\frac{(1-\alpha^3)B_9\,\Phi_a^*\,\Lambda_a\,\Omega_a(1-x_{oa})}{(1-B_5(1-x_{oa})\Omega a)} + \frac{\alpha^3 B_9 S_a^{\circ 2}\Phi_a^*\,\Gamma^2(1-x_{oa})}{4\pi L_a^\circ V_a^\circ(1-B_5(1-x_{oa})\Omega_a)} \qquad 2.37$$

where $B_5 = V_a^\circ\,\rho^\circ_{B_{oa}}$, $B_6 = \rho^\circ_{B_{oa}}/\rho^\circ_{B_i}$

$B_7 = K_a M_B C_g^{\frac{1}{2}} S_a^\circ$, $B_8 = 2.0\pi K_a M_B C_g^{\frac{1}{2}} L_a^\circ / S_a^\circ\,\rho^\circ_{B_{oa}}$

$B_9 = \phi_a^\circ L_a^\circ\,\rho^\circ_{B_{oa}}/\bar{l}_a$

$\Phi_a^* = \phi_a/\phi_a^\circ = 1/(1-x_{oa})^{n_a}$

and the initial combination rate function, ϕ_a°, was related to the initial macropore growth rate.

$$\phi_a^\circ = \epsilon_a B_7 \qquad 4.7$$

ϵ_a is the proportionality constant.

The internal conversion as defined by equation 2.13 was obtained in terms of the macropore volume and micropore conversion by combining equations 2.13 and 2.14.

$$x_{oa} = 1 - \frac{1}{\rho^\circ_{B_{oa}}\left(V_a^\circ\Omega_a + \frac{1}{\rho^\circ_{B_i}(1-x_i)}\right)} \qquad 4.8$$

The differential equations, 2.21, 2.22, 2.35, 2.36, 2.37 and 4.4 were numerically integrated to obtain the properties and micropore conversion as a function of time, and equations 4.1 and 4.8 were used to obtain the internal and overall conversion.

These equations used a total of twenty-two constants and parameters. Fourteen of these were obtained from the initial properties of the material or from the assumed structure, and eight were obtained by non-linear least squares analysis of the data from the micro-balance and the fluidized bed.

The fourteen parameters obtained from initial analysis of the samples are summarized in Table 4.5. The macropore volume, V_a°, and the overall apparent density, $\rho_{B_{oa}}$ were determined by mercury porosimetry. The micropore volume, V_i°, was measured by nitrogen adsorption. The true density, ρ_t, was calculated from equation 2.13 and the initial micropore density by equation 2.15. The micropore surface area, which was assumed to be the total measured by nitrogen adsorption, was measured by nitrogen adsorption and calculated by the methods proposed by Dollimore and Heal.[2] The initial micropore surface area was obtained by extrapolating the values obtained at low conversion back to zero. However, for the pelletized material this suggested an area of only 100 m^2/gm. This was because a large amount of the pore volume was in voids that was not accessible by mercury or nitrogen. If the 100 m^2/gm is used, the slit pore geometry gives the initial mean pore radius as:

$$r_i = \frac{V_i^\circ}{S_i^\circ} = 8.7 \text{ Å} \qquad 4.9$$

The pore distribution data showed the mean pore was less than 5 Å. An initial mean pore radius of 3.35 Å, which is two times the minimum spacing was assumed and by applying equation 4.9, the initial surface area became 520 m^2/gm. The surface area of one plane, s_i, and the pore radius of an initiated pore, r_f, were obtained from the structure assumed from the crystallite. The radius of an initiated pore, r_f, was assumed to be half

TABLE 4.5

PARAMETERS DETERMINED FROM INITIAL DATA

Parameter	Pelletized	Non-Pelletized	Units
V_a°	0.12	0.155	cm^3/gm
V_i°	0.174	0.1553	cm^3/gm
$\rho^\circ_{B_{oa}}$	1.19	1.1375	gm/cm^3
$\rho^\circ_{B_i}$	1.388	1.381	gm/cm^3
ρ_t	1.83	1.758	gm/cm^3
S_a°	2.00	3.00	m^2/gm
$\bar{l}$	10^{-4}	10^{-4}	cm
s_i	475.3	475.3	$Å^2$
S_i°	520.0	777.0	m^2/gm
r_f	1.675	1.675	Å
R_a°	1.2×10^{-5}	1.033×10^{-5}	cm
L_a°	2.65×10^{8}	4.62×10^{8}	cm
R_p	0.0538	0.0538	cm
α	0.5	0.5	

the spacing between two layers in the crystallite (1.675Å). The surface area of one plane, s_i, depends on the diameter of the crystallite. The crystallite was assumed to be cylindrical with the diameter approximately the same as the height or the number of layers. The crystallite was assumed to be 7 to 10 layers thick (23.5Å to 33.5Å), therefore the crystallite diameter was assumed to be 24.6Å. This results in a layer surface area of $475.3 Å^2$.

The mean macropore radius for the pelletized material was determined from the mercury porosimeter and was 1200Å. The non-pelletized had a flat distribution of pore sizes, so the mean pore radius was assumed to be 1033Å. These values and the corresponding macropore volumes were used to calculate the total macropore surface area and total macropore length. The mean macropore length for a single pore was assumed to be 10^{-4} cm, which is the diameter of the subparticles in the pelletized material. These parameters for the macropores were not critical. The combination parameter, α, which is defined in equation 2.27 was assumed to be 0.5 for both the pelletized and non-pelletized samples. This was a good assumption for a narrow distribution of pore sizes, which was present in the pelletized materials but may have been a little low for the non-pelletized sample.

There were a total of eight parameters determined by non-linear least squares analysis of the combined data from the micro-balance and the fluidized bed. There were four from the micropore equations and four from the macropore and external burn-off equations. The micropores were fit independently from the macropores. The four parameters for the micropores were K_i, K_f, n_i and ϵ_i. K_i and K_f were the rate constants for pore growth and pore initiation and were used in determining the coefficients

B_1 and B_2 in equation 2.22. The dimensionless coefficient B_2 was much greater than B_1 making it impossible to determine K_i. Consequently, K_i was neglected in all the other calculations. The pore initiation rate constant, K_f, was determined from a fit of all the rate data. The rate constants were fit to an Arrhenius type rate expression:

$$K_f = C_i \exp(-E_{ai}/RT) \qquad 4.10$$

where C_i is the pre-exponential factor and E_{ai} is the activation energy. The pelletized and non-pelletized material are shown in Figure 4.1. The pelletized material had a better fit than the non-pelletized material. This was probably because of the approximation of the Langmuir rate expression by a half-order expression. However, the rates were very similar and the activation energies were very close, indicating that the reaction mechanisms for the crystallites were approximately the same (See Table 4.6). The micropore surface area was defined by equation 2.21 and the only parameters to be determined were the parameters related to the pore combination function, ϵ_i, and n_i. The exponent, n_i, for the pore combination function was assumed to be 1.0, which was the same as for Hashimoto and Miura.[3] The actual value was not critical, because the overall magnitude was determined by ϵ_i. The important characteristic of the relative combination function was that it approached ∞ as the reaction reached completion. These values are summarized in Table 4.6.

There were three parameters for the macropores, K_a, n_a and ϵ_a, and one for the external burn-off of the particle, F. The equations for the macropores had to be integrated simultaneously with the micropore equations because the macropore equations involve both the micropore conversion rate and the micropore conversion. The macropore rate constant, K_a

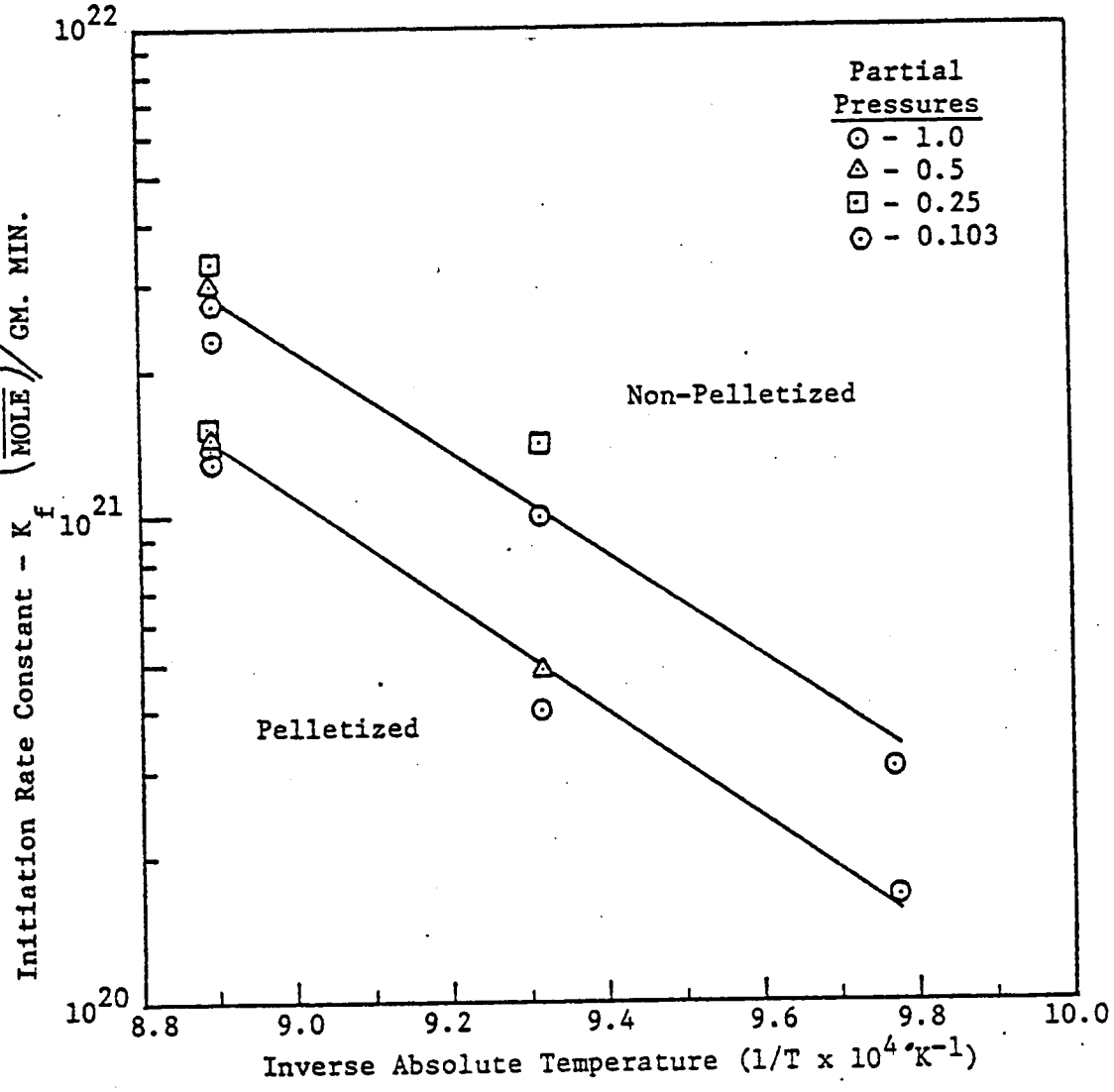


Figure 4.1. Arrhenius Plot for Micropore Initiation Rate Constant.

TABLE 4.6

PARAMETERS DETERMINED FROM NON-LINEAR LEAST SQUARES ANALYSIS OF THE RATE AND PORE STRUCTURE DATA

Parameter	Pelletized	Non-Pelletized	Units
$K_f - C_i$	8.66×10^{30}	6.04×10^{30}	$\frac{\left(\frac{cm^3}{mole}\right)^{\frac{1}{2}}}{gm.min}$
$K_f - E_{ai}$	50,400	48,000	$\frac{cal}{gm.mole}$
$K_a - C_a$	6.87×10^{6}	2.52×10^{1}	$\frac{\left(\frac{mole}{cm}\right)^{\frac{1}{2}}}{min}$
$K_a - E_{aa}$	56,000	37,700	$\frac{cal}{gm.mole}$
ϵ_i	2.38×10^{-20}	1.44×10^{-20}	cm^3
n_i	1.0	1.0	
ϵ_a	5.73×10^{-13}	3.64×10^{-14}	cm^3
n_a	2.0	1.0	
F	21	1000	

was also fit to an Arrhenius type rate expression:

$$K_a = C_a \exp(-E_{aa}/RT) \qquad 4.11$$

where C_a is the pre-exponential factor and E_{aa} is the activation energy (See Figure 4.2). These rate constants for the non-pelletized and pelletized material were not in as good an agreement as the values for the micropores. The pelletized material had a much higher reaction rate, which could be due to either the pelletizing or the binder. The pelletized material had a larger ash content which could have come from the use of pulp waste as the binder. The ash content could have had a catalytic effect on the reaction. The pore combination parameters, ϵ_a and n_a, were also obtained from a fit of all the data. As in the micropores, n_a was not very critical and so was rounded to the nearest whole number. These parameters are summarized in Table 4.6, p. 47.

These parameters allowed the micropore and macropore properties and the internal conversion to be obtained. Initially equation 4.2 was used to obtain the external burn-off of the particle, but this rigid sphere model greatly underestimated the real rate. Equation 4.4 was used and F was determined from the fit with the data (See Table 4.6, p. 47).

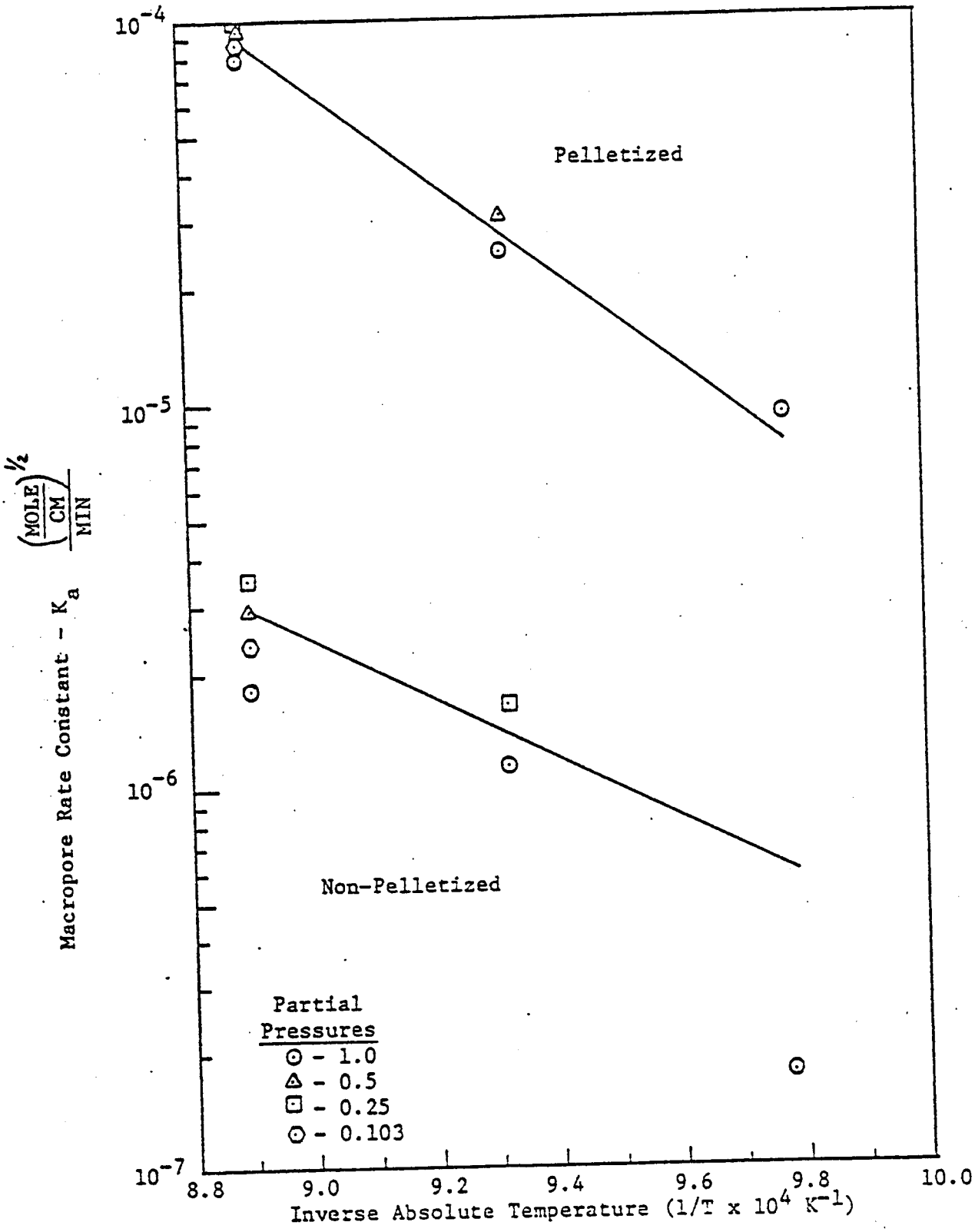


Figure 4.2. Arrhenius Plot for Macropore Rate Constant.

C. COMPARISON OF THE FINAL EQUATIONS TO THE MEASURED VARIABLES

The parameters listed in Table 4.5, p. 43 and Table 4.6, p. 47 were used in the equations given in Chapter IV, Part B. Those equations were numerically integrated using the Runge-Kutta Gill method. They were solved for the same conditions as were investigated in the micro-balance.

The curve for micropore conversion, x_i, was linear because the value of K_i was small (See Figures 4.3 and 4.4). This states that the rate of initiation was much greater than the rate of pore growth. It has been assumed that the crystallite structure was very similar to graphite. West[19] stated that the end burning of graphite crystallites was an important mechanism in the graphite - CO_2 reaction. This leads us to believe that this edge burning mechanism of the crystallite is related to the initiation mechanism. The data did not show an increase in reaction rate which would have been present if the pore growth rate constant K_i, which was directly related to the surface area, had been significant. The rate decreased by $(1-x_i)$ until 50 percent micropore conversion, which was predicted by equation 2.22. However, beyond 50 percent micropore conversion the rate decreased more rapidly. This could be due to the fact that the initiation reaction was assumed to be independent of the surface area, and it only depended on the amount of material present. A different reaction rate at higher conversions might be achieved, if the initiation reaction was related to the external area of the crystallites or was dependent upon certain active sites which become deactivated at a higher rate than $(1-x_i)$. These possibilities were also supported by the fact that both the pelletized and non-pelletized material showed the same characteristic, decrease in rate.

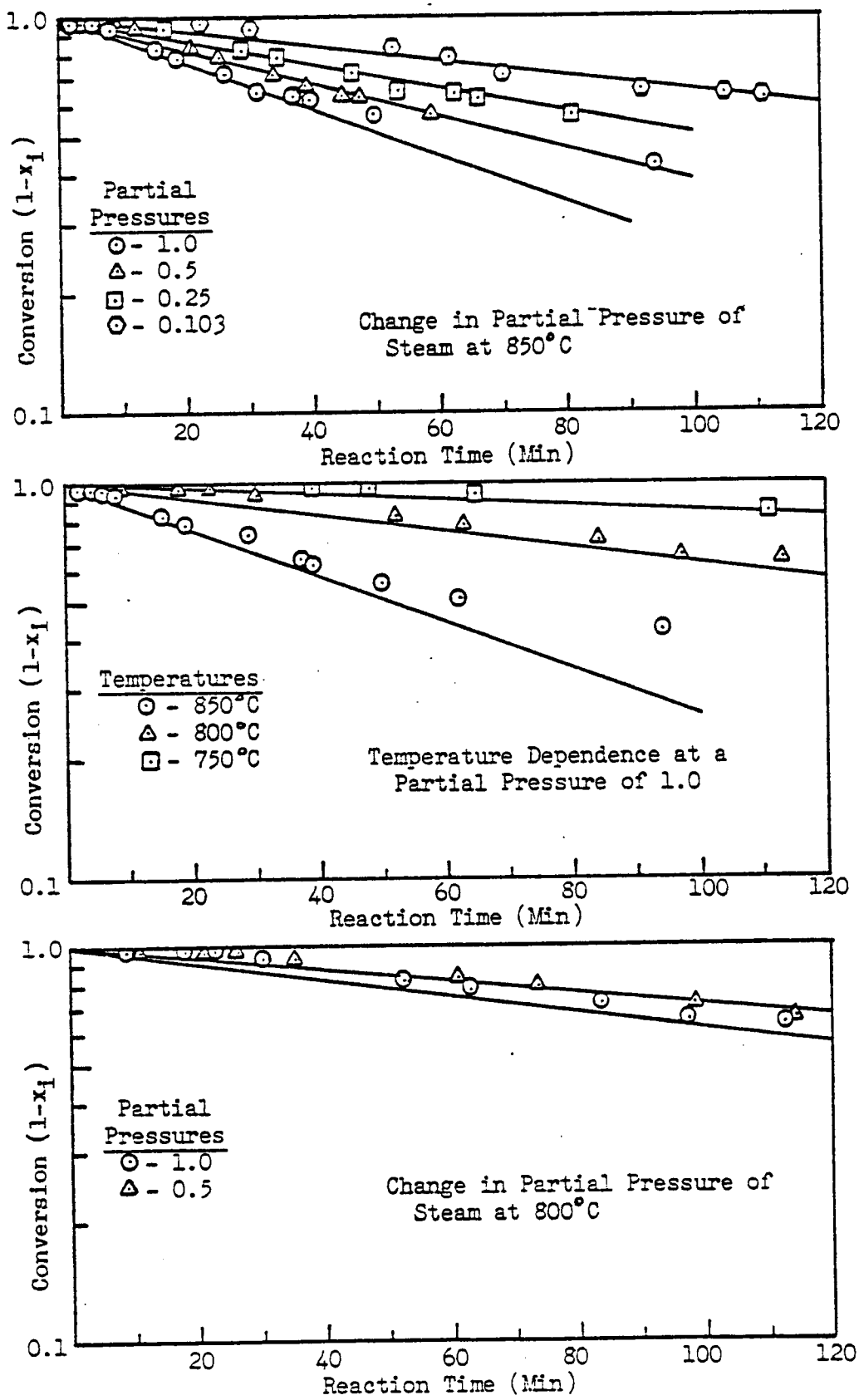


Figure 4.3. Micropore Conversion for Pelletized Coal.

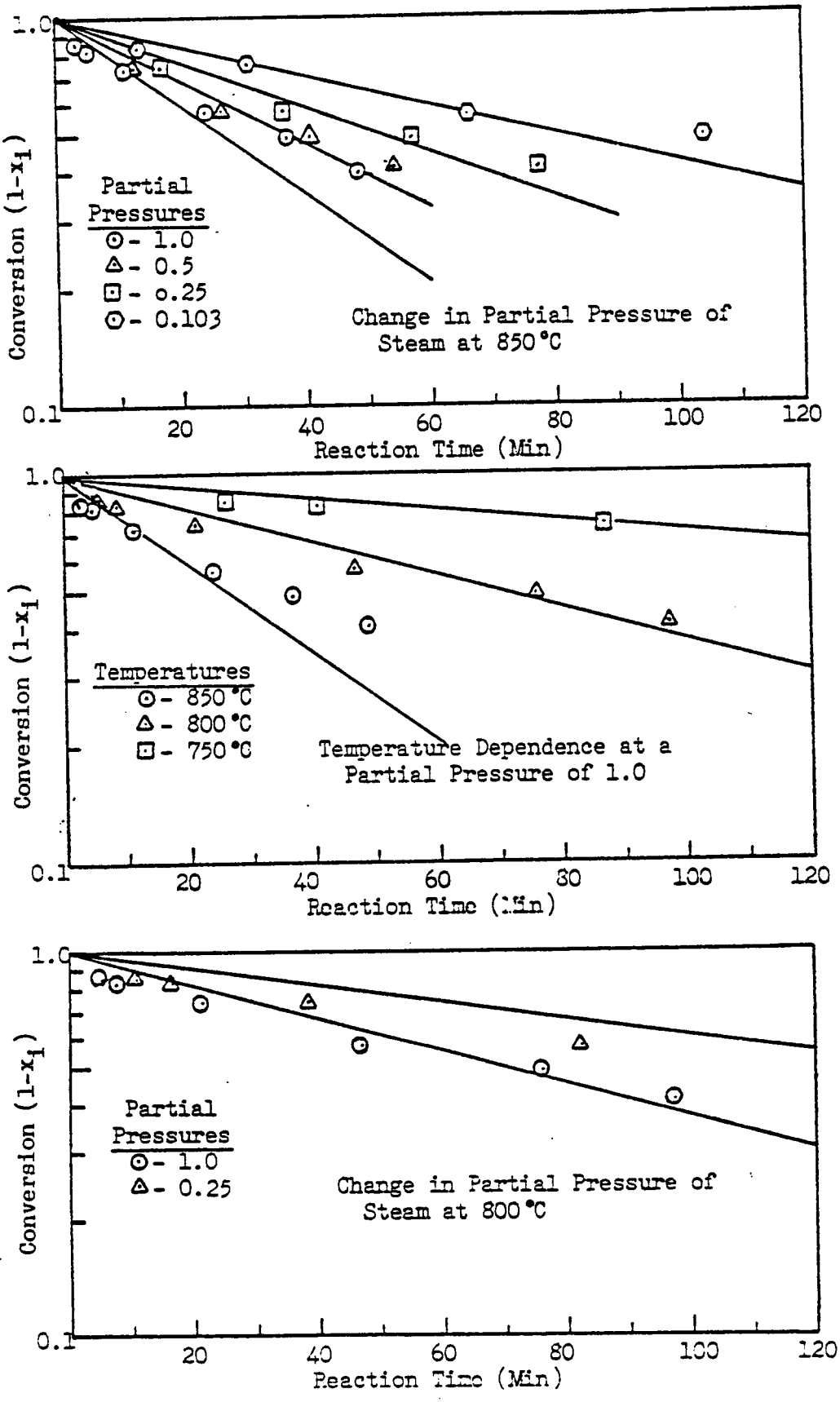


Figure 4.4. Micropore Conversion for Non-Pelletized Coal.

The internal conversion was obtained from equation 4.8. The rate was dependent on both the micropore and the macropore conversion rates. The curves, Figures 4.5 and 4.6, for the pelletized and the non-pelletized did not demonstrate the similarity as in the micropore conversion. This was the result of the difference in the macropore development. The pelletized material in Figure 4.5 had a very high initial rate which decreased rapidly until about 20 to 30 percent burn-off and then becomes almost linear. The opposite was true for the non-pelletized material. It was almost linear for the first 50 to 60 percent burn-off and then begins to increase in rate. Since the micropore rates decreased linearly, the unusual shape of the internal conversion curves had to be due to the macropores. In fitting the macropore data, the macropore volume was weighted more than the surface or length because these values were not directly measured and were not as important as the volume. In any case, the figures presented on pp. 64-65, show that both the samples gave good fits on the volume data, and the non-pelletized material agreed well with the surface area and length. However, the pelletized material did not fit well with the data for the surface area or the length. The rapid decrease in the macropore surface area calculated for the pelletized material was due to the fact that the program was trying to fit the rate data and the only way to get the rapid decrease in the reaction rate for the pelletized material was by decreasing the surface area through the coalescence of the macropores. The coalescence does not affect the volume but does affect the surface area and length.

There are three possible explanations for the discrepencies between the measured data and the calculated data for the pelletized material. The first is that the cylindrical shaped pore assumption is not valid.

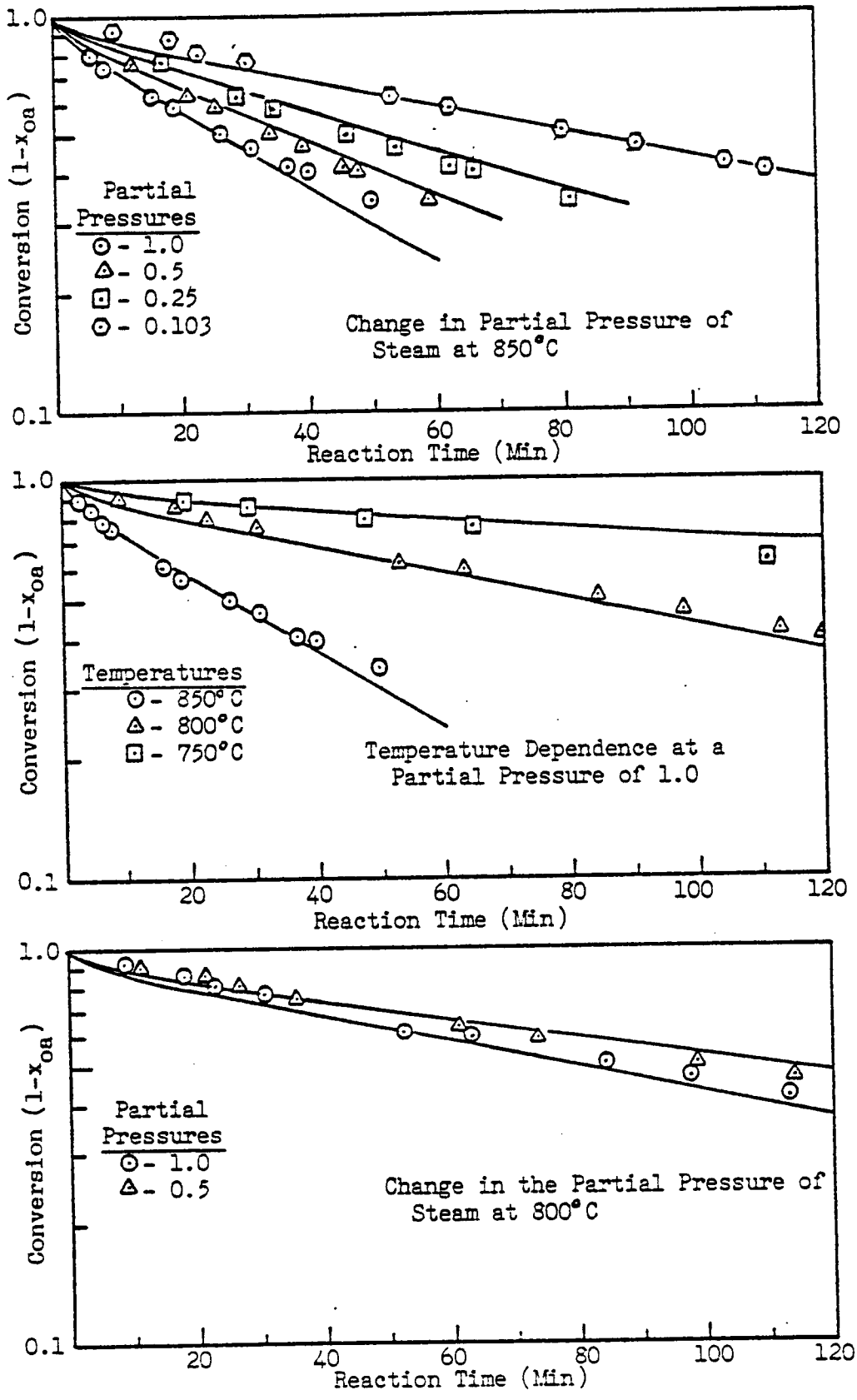
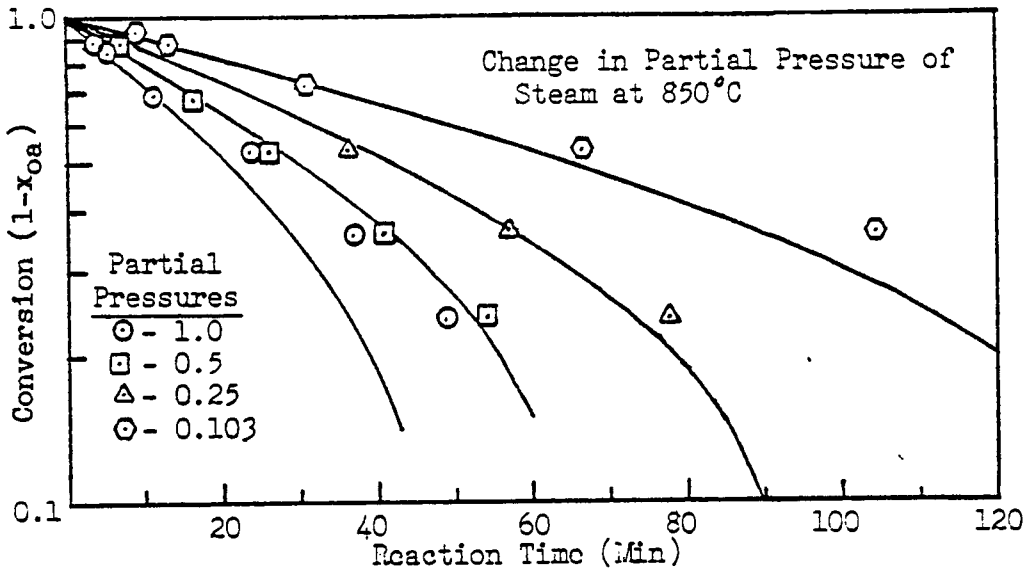
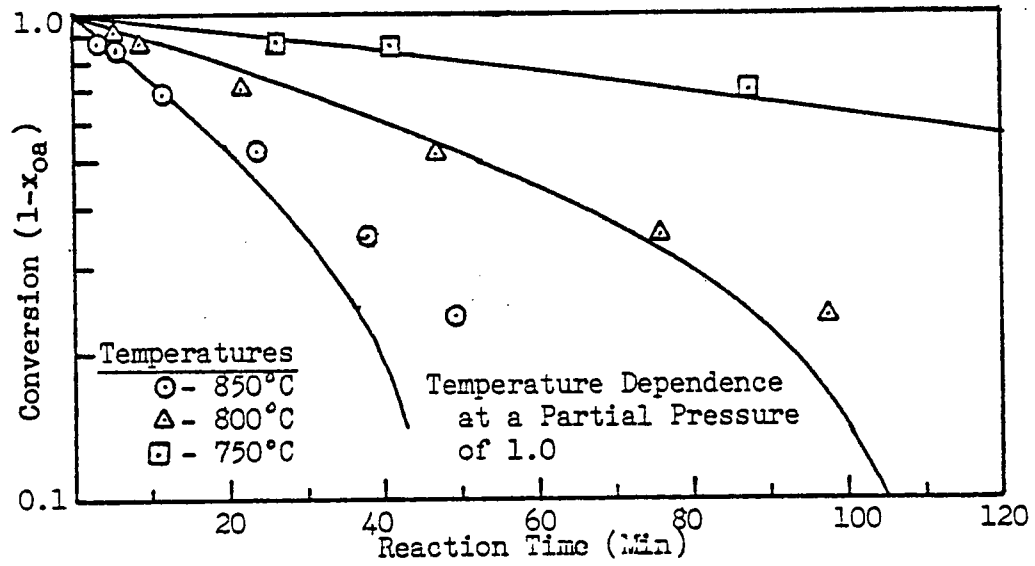


Figure 4.5. Internal Conversion for Pelletized Coal.





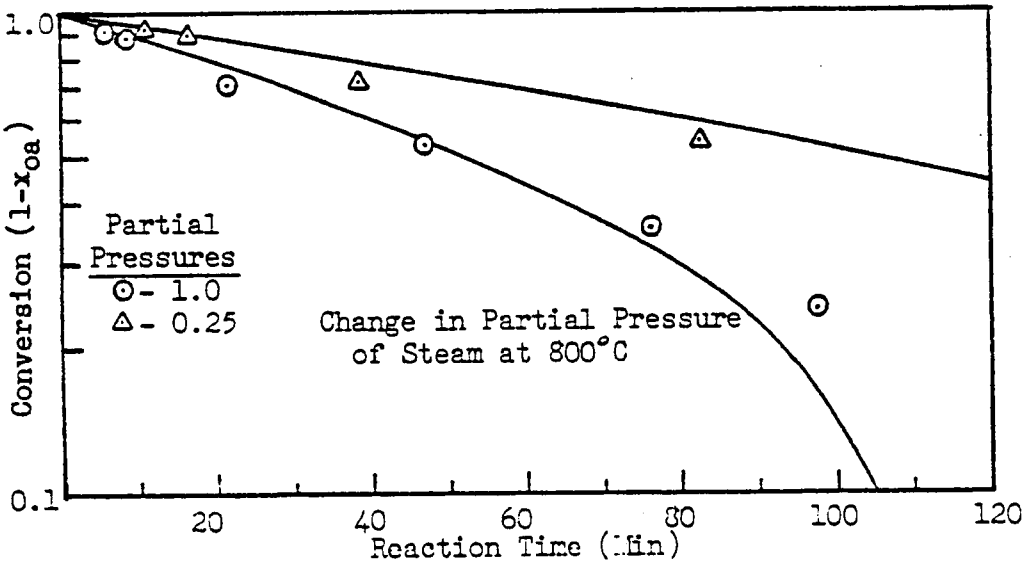


Figure 4.6. Internal Conversion for Non-Pelletized Coal.

Pores of another geometry would have a different surface area to volume ratio and the pore distribution data from the mercury penetration analysis would be different. This is not a good explanation because many people have used the cylindrical shape and obtained good results.[9,19] Also, the non-pelletized coal char, using the cylindrical shape, fit the data well. The second possible explanation is the presence of different amounts of amorphous carbon. The micropores have been restricted to the crystalline material. Therefore, the macropores should consist of the crystalline and amorphous carbon and if the amorphous carbon had a lower activation energy, then it would react faster initially. However, the difference in rates may not be as great as was seen in the pelletized material and the non-pelletized material did not show this characteristic. The third possibility is a catalytic effect from the ash. The pelletized material had a much higher ash content (13.82 percent) than the non-pelletized material (2.79 percent). Rand and Marsh[10] have shown that the addition of small amounts of iron to polyfurfuryl alcohol catalyzed the reaction with CO_2 and that the catalytic effect of the iron became inactive after about 15 percent burn-off. This type catalytic reaction could explain the rapid decrease in the reaction rate. If this was true, then the macropore surface area for the pelletized material shown in Figure 4.13 p. 65 (from equation 2.36) was the effective surface area not the total macropore surface area. Using this active site approach, Figure 4.13 would represent the relative number of active sites. If one multiplies these by $(1-x_f)$ to obtain the values relative to the initial sample weight, then the non-pelletized material in this case, the non-catalytic material, would show almost a flat line indicating that the number of active sites per unit of initial sample weight remains constant. However, the

pelletized material in this case, the catalyzed material, would show a very rapid decrease in the number of active sites.

The non-pelletized material also showed an increase in rate above 60 percent internal conversion (See Figure 4.6, p. 55). This was primarily due to the decrease in the apparent density and the increase in macropore surface area.

The overall conversion, x_f, was calculated by equation 4.1 using the internal conversion previously calculated and the particle shrinkage obtained from the integration of equation 4.4. These are shown for the pelletized and non-pelletized material in Figures 4.7 and 4.8 respectively. The fit was good for both the samples at all the different experimental conditions. The data points shown in the figures were obtained from the micro-balance.

The relative particle radius, ξ, from the data by Imai[6] and Yoshikawa[20] was calculated from equation 4.1. The overall conversion, x_f, was determined from the overall weight loss. The internal conversion, x_{oa}, was determined from the particle porosity, which was obtained from the mercury porosimeter at one atmosphere pressure. At one atmosphere pressure all pores greater than 1.2×10^{-2} mm diameter are filled with mercury, therefore they are assumed to be part of the external structure of the particle. This means that the relative particle radius was a combination of the particle shrinkage and the growth of all pores greater than 1.2×10^{-2} mm diameter. The relative particle radius is shown in the figure on p. 66. The fit was very good after the correction factor, F, was determined. The large values of F can be partially justified by looking at the electron scanning micrographs in Appendix D, which show that both particles were far from rigid spheres and that there are

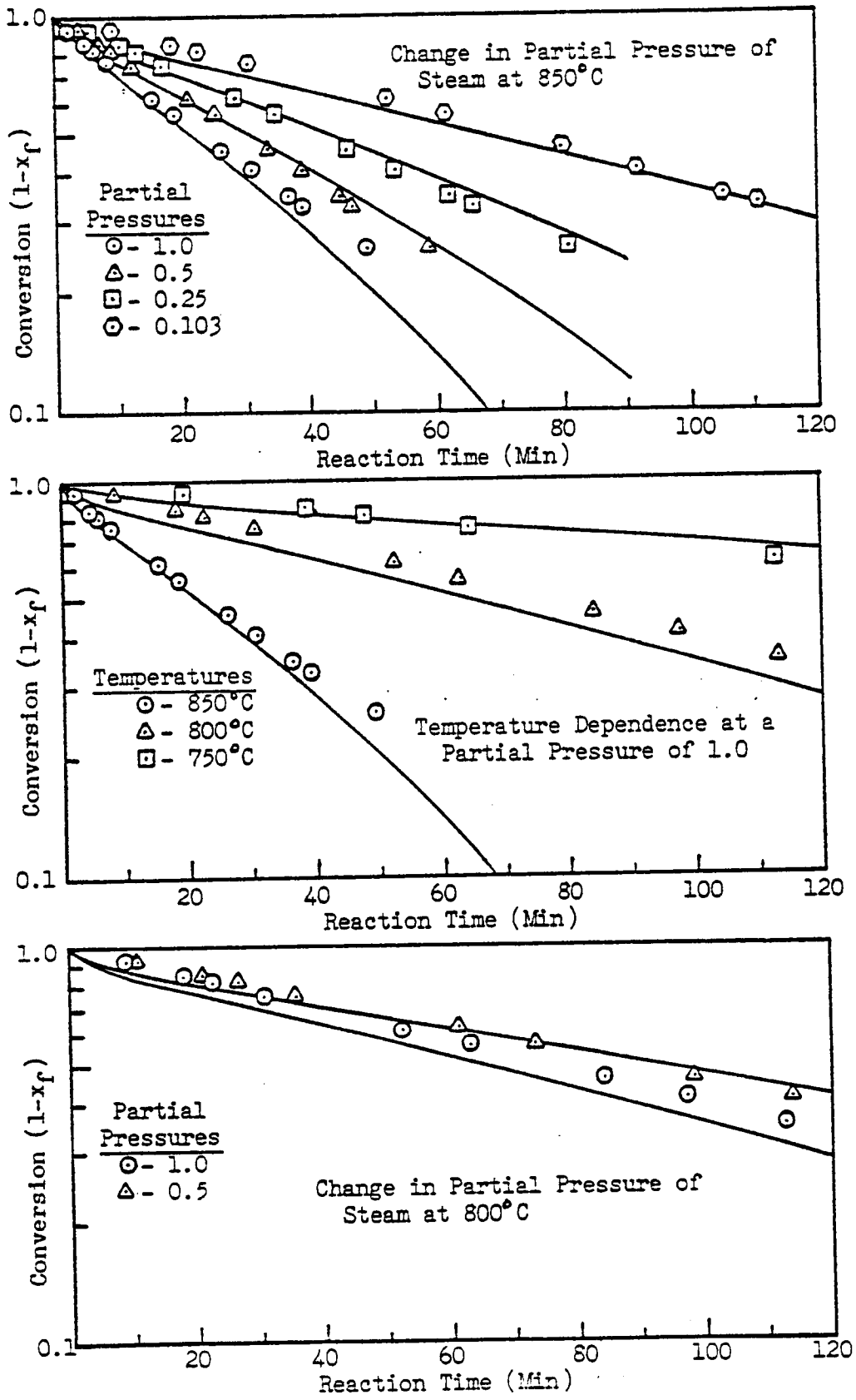
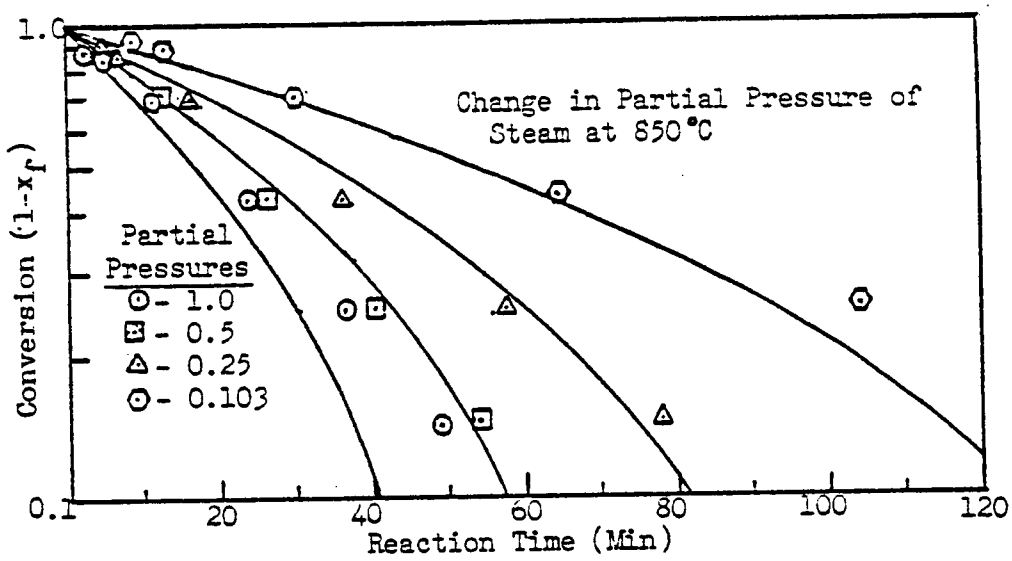
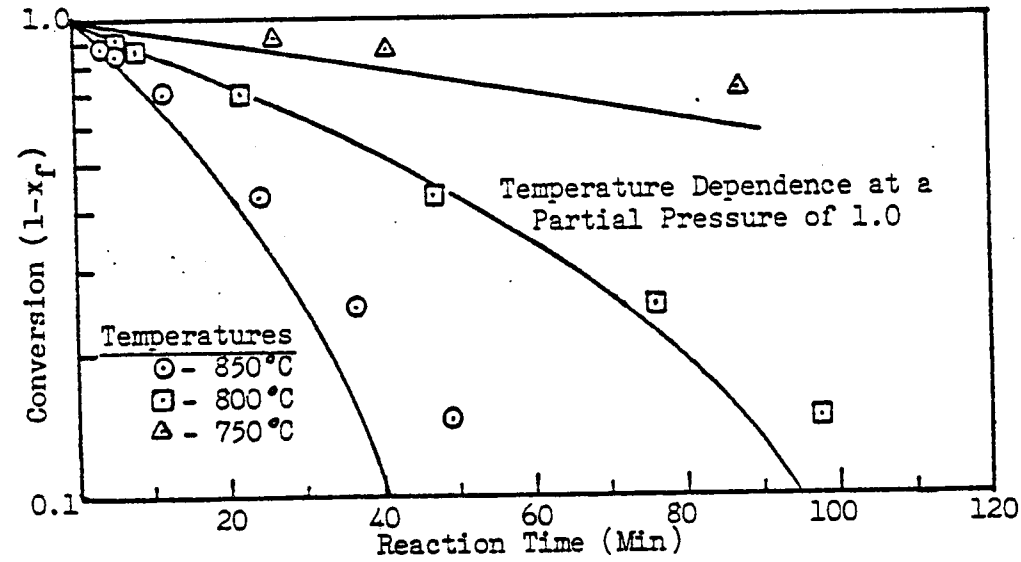


Figure 4.7. Overall Conversion for Pelletized Coal.





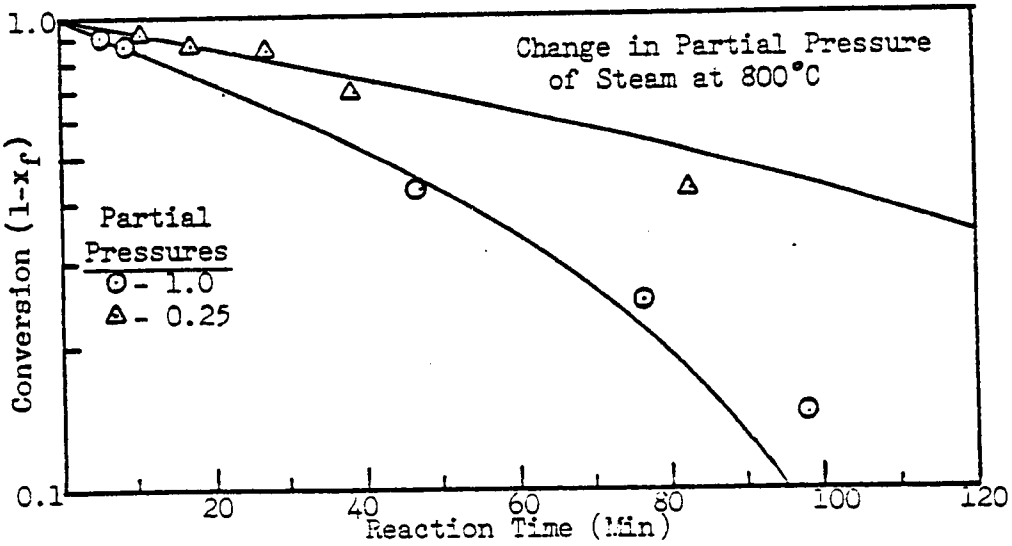


Figure 4.8. Overall Conversion for Non-Pelletized Coal.

considerable number of pores and voids with radii greater than 1.2×10^{-2} mm diameter.

The various pore structure properties as a function of conversion were obtained from the fluidized bed experiments by Imai[6] and Yoshikawa[20]. These were combined with the micro-balance data to give the properties as a function of time, which were used in the determining of the parameters. All the differential equations for the properties and conversions were integrated with respect to time. Using the overall conversion as a base, one can obtain the properties and conversions obtained from the differential equations as a function of the overall conversion, which then corresponds to the data from Imai[6] and Yoshikawa[20]. These are shown in Figures 4.9 to 4.15. The curves are for a reaction temperature of 850°C and 1.0 atm. partial pressure of steam. There was only a slight shift in the curves at different temperatures due to the different activation energies of the rate constants.

The micropore conversion shown in Figure 4.9 and the relative macropore volume shown in Figure 4.12 help to explain some of the differences between the pelletized and non-pelletized samples. A greater percentage of the non-pelletized material's conversion occurred in the micropores than in the macropores and the opposite was true for the pelletized material.

The micropore surface areas are shown in Figure 4.10. Neither of the samples showed a maximum in the surface area, however, if the areas were determined using the initial sample weight and not the actual weight both would show a maximum at approximately 20 percent overall conversion. This is interesting because West[19] had observed in the CO_2 activation of coal char that the micropores grow very little during activation and the

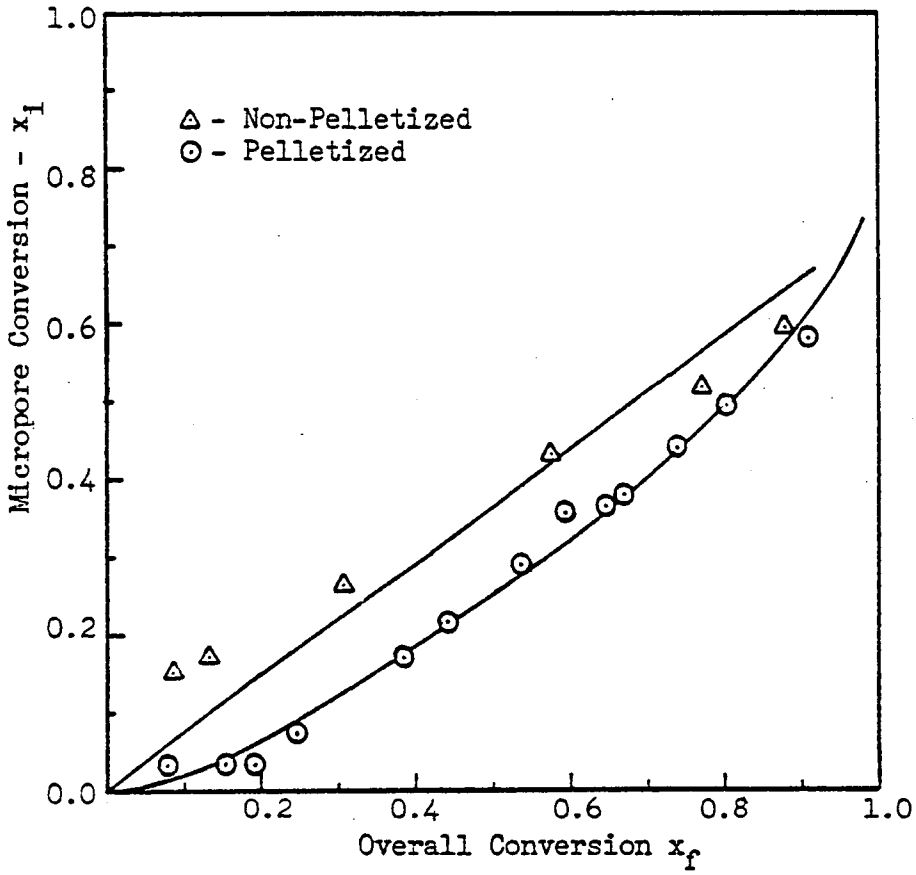


Figure 4.9. Micropore Conversion versus Overall Conversion.

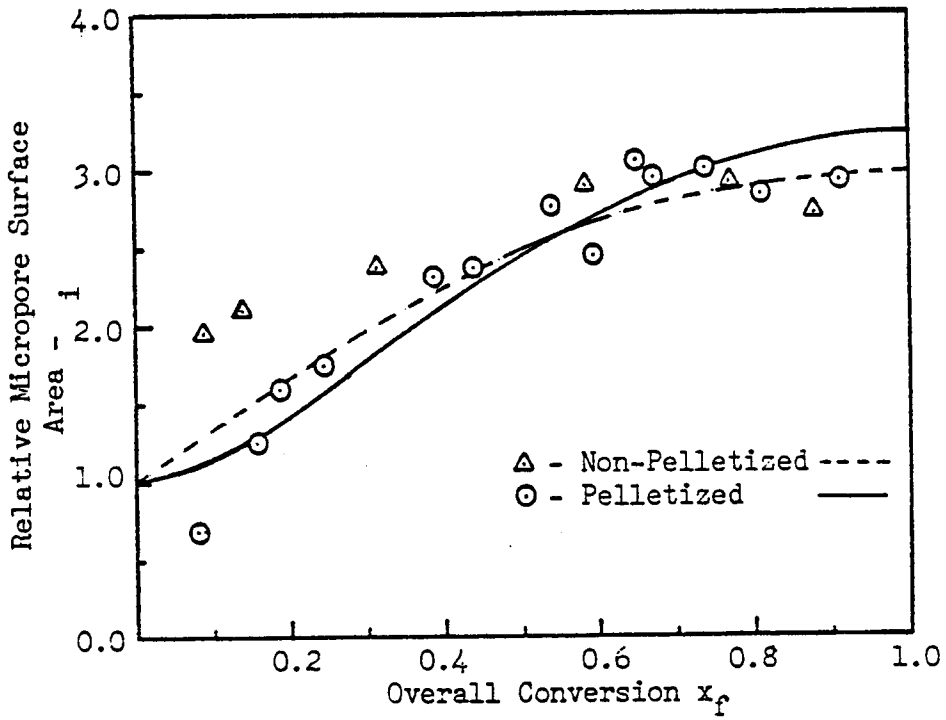


Figure 4.10. Relative Micropore Surface Area versus Overall Conversion.

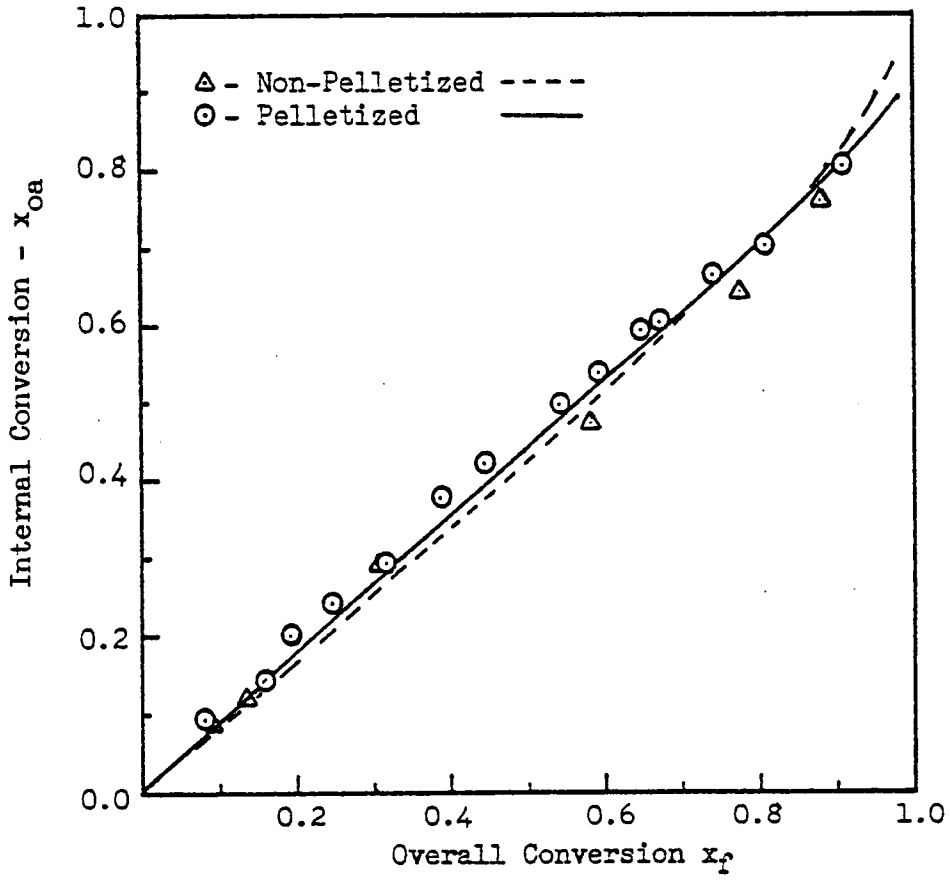


Figure 4.11. Internal Conversion versus Overall Conversion.

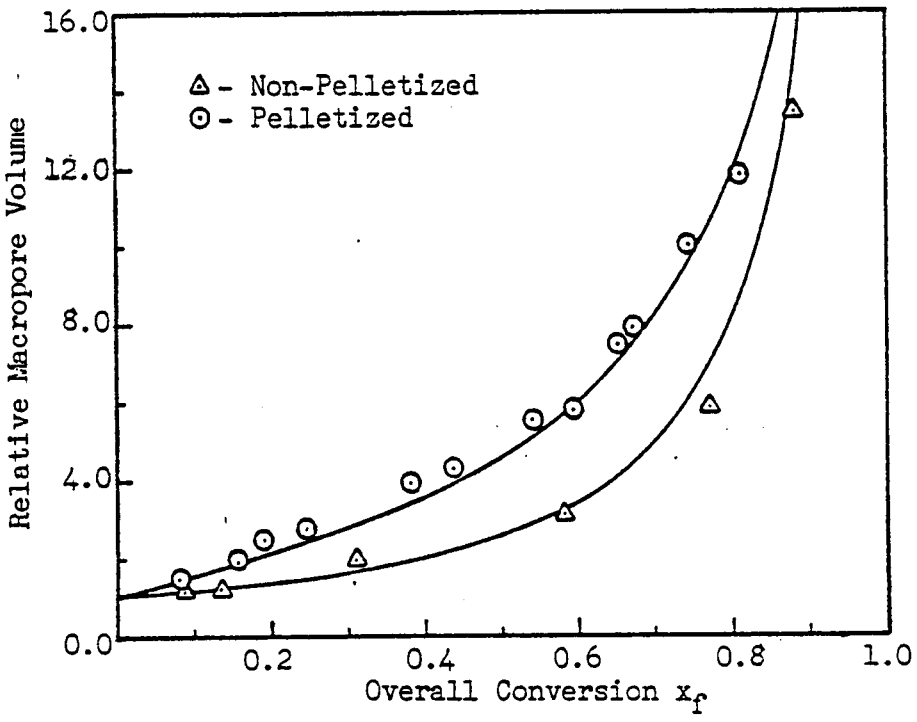


Figure 4.12. Relative Macropore Volume versus Overall Conversion.

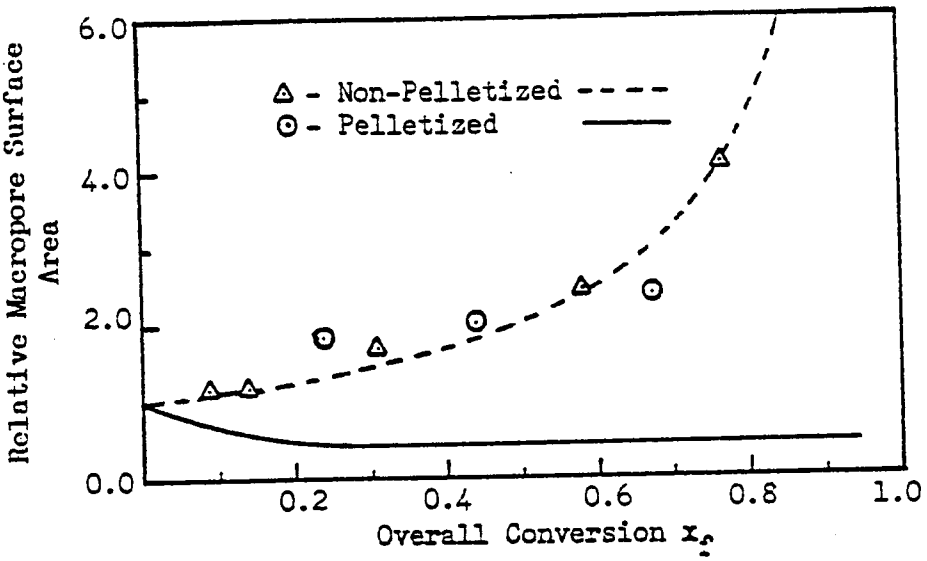


Figure 4.13. Relative Macropore Surface Area versus Overall Conversion.

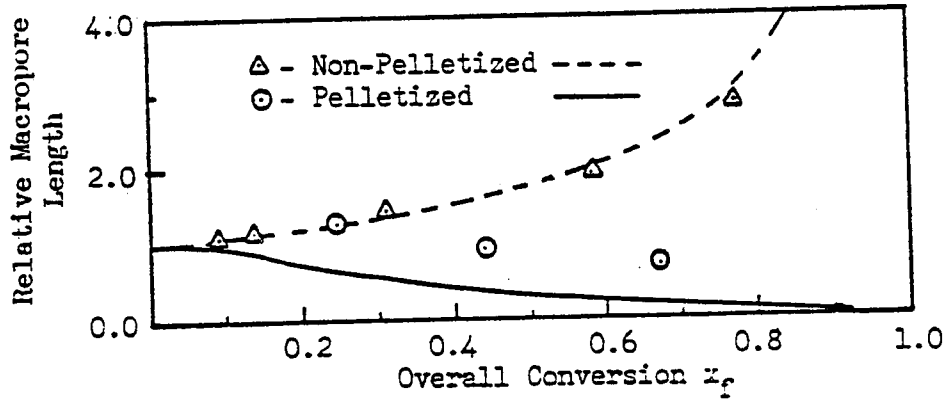


Figure 4.14. Relative Macropore Length versus Overall Conversion.

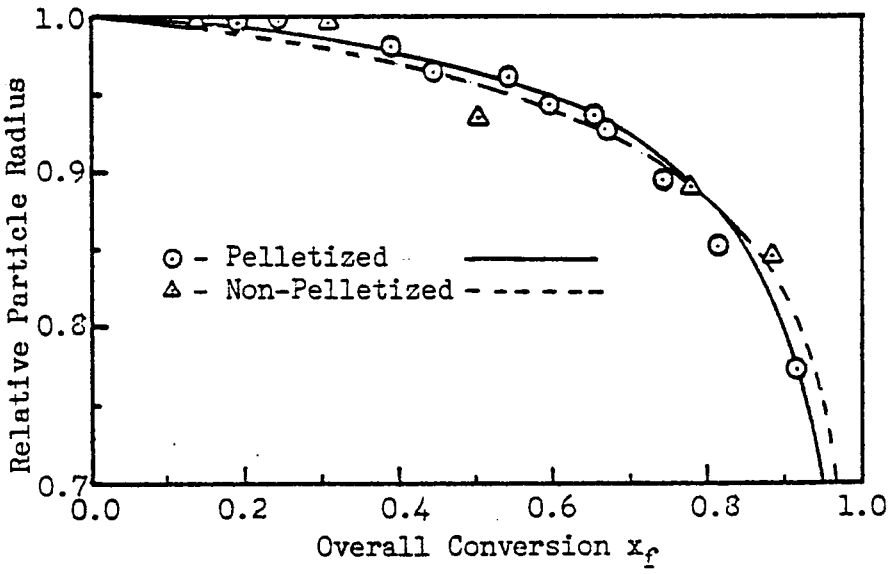


Figure 4.15. Relative Particle Radius versus Overall Conversion.

increase in volume and surface area was the opening of closed pores. Even though our steam activated samples showed considerable micropore growth, the optimum extent of conversion was the point by which most of the closed pores were opened which was 15 to 20 percent conversion.

Figure 4.11 p. 63 shows the relationship between the internal conversion and the overall conversion. Up through 50 to 60 percent overall conversion, the reaction was almost entirely confined to the interior of the particle. This can also be seen in Figure 4.15 p. 68 for the relative particle radius. The shrinkage was very small until beyond 50 percent conversion.

The macropore properties are shown in Figures 4.12, 4.13 and 4.14 pp. 64-65. As explained before, the macropore volume was the primary property fit in the non-linear least square analysis of the macropore data. The data for the macropore surface area and length were calculated from the volume data using the cylindrical shape pore geometry and a few mean macropore radii from the mercury porosimeter for the pelletized material. For the non-pelletized material, it was assumed that coalescence was small, therefore the total macropore length would be a constant with respect to the initial amount of material. This gives the relative macropore length and surface area as:

$$\Lambda_a = 1/(1-x_{oa}) \qquad 4.12$$

$$\Gamma_a = \sqrt{\Lambda_a \Omega_a} \qquad 4.13$$

The non-pelletized material fit this assumption very well. The pelletized material was not able to fit the surface area and length data. This was most likely due to the pelletizing, which either changed the ash content, which catalyzed the reaction or changed the mechanism of coalescence.

CHAPTER V

CONCLUSIONS AND RECOMMENDATIONS

A. CONCLUSIONS

The proposed combined model for micropores and macropores fits the rate and pore structure development very well, as can be seen from Figures 4.3 to 4.15 pp. 51-66. This bimodal model suggests the possibility that the micropores and macropores may develop by different mechanisms. The micropore rate was not greatly dependent upon the surface area, while the macropore rate was dependent upon the surface area (or perhaps to certain active sites).

The micropore rate was independent of the surface area because the rate constant, K_i, was small. The initiation rate was the major contribution to the micropore conversion, and this was assumed to be independent of the surface area. The initiation rate constants, K_f, for the pelletized and non-pelletized samples had similar values and their activation energies were about the same (50,400 cal/gm.mole and 48,000 cal/gm.mole). Also, the micropore surface area development was successfully modeled (Figure 4.10, p. 62). Thus, the mechanism for micropore initiation involving the etching type action to remove a single layer seems reasonable for the micropore development. Also, if the system is kinetically controlled the pelletization, which is a macroscopic process, should not affect the micropore development.

The macropores did not show these similarities between the pelletized and non-pelletized materials. Most of the differences in gasification rate and pore development at this level are due to the pelletization of

one of the coal chars. The pelletizing process could cause these effects by (1) the physical process of pelletization and addition of the binder, or (2) the catalytic action of the ash from the binder. The latter seems better because the rate data for the pelletized coal char showed the same characteristic high initial rate as the catalytic effect in a different system (involving the effect of iron on the polyfurfuryl carbon-carbon dioxide reaction[10]).

B. RECOMMENDATIONS

The model as developed in this thesis involved several assumptions and approximations. Further study should be conducted to eliminate or refine them as follows.

The micropores were assumed to be only in crystallites. Their dimensions depended upon the crystallite size, which can vary greatly between coal chars. Therefore, the dimensions should be determined by x-ray analysis of the individual coal chars. The two coal chars investigated in this thesis showed similar rate constants and activation energies for the micropores. Further investigation of other coal chars should be attempted to see if this similarity in activation energies is universal for other coal chars of similar nature. Also, the Langmuir type rate expressions for the micropores and macropores were approximated as half-order rate expressions. An increase in the number of experiments at other temperatures and pressures should be used to determine the true rate constants.

The macropore development which was greatly affected by the pelletizing of the coal chars should be investigated in more detail. Further

study should incorporate the use of the scanning electron microscope to study the actual shape of the macropores and how they develop. Also, the investigation of the catalytic effects of the ash (binder) should be conducted (possibly in procedure similar to the one by Marsh and Rand[10]). This would be of dual importance. The catalytic effect would be of importance in coal gasification or liquefaction and in the fluidized bed combustion of coal. The micropore development (surface area) is of prime importance in the production of activated carbons. Macropore and external gasification are undesirable, so the use of a poison to deactivate the catalyst would be helpful.

The equations developed from the population balance equation for describing the change in these particles are not restricted to the carbon-steam reaction. They can be applied to other heterogeneous reactions occurring in porous solids where the structure can change significantly during the course of the reaction, as in the case of the hydrochloric acid-limestone reaction studied by Schechter and Gidley[12].

LIST OF REFERENCES

LIST OF REFERENCES

1. Blyholder, G. and H. Eyring, "Kinetics of Graphite Oxidation," Journal of Physical Chemistry, 61, (May 1957), 682.

2. Dollimore, D. and G.R. Heal, "An Improved Method for the Calculation of Pore Size Distribution From Adsorption Data," Journal of Applied Chemistry, 14, (March 1964), 109.

3. Hashimoto, Kenji and Kouchi Miura, to be published.

4. Hashimoto, Kenji and P.L. Silveston, "Gasification: Part 1. Isothermal, Kinetic Control Model for a Solid with a Pore Size Distribution," AIChE Journal, 19, (March 1973), 259.

5. Hashimoto, Kenji and P.L. Silveston, "Gasification: Part 2. Extension to Diffusion Control," AIChE Journal, 19, (March 1973), 268.

6. Imai, Ichiro, "Change in the Pore Structure During Steam Activation of Coal Char," Masters of Science, Kyoto University: Kyoto, Japan, (March 1973).

7. Lamond, T.G. and H. Marsh, "The Surface Properties of Carbon-III. The Process of Activation of Carbons," Carbon, 1, (April 1964), 293.

8. Mattson, James S. and Harry Mark. Activated Carbon: Surface Chemistry and Adsorption From Solution. New York: Marcel Dekker, Inc., 1971.

9. Petersen, E.E., "Reaction of Porous Solids," AIChE Journal, 3, (December 1957), 443.

10. Rand, B. and H. Marsh, "The Process of Activation of Carbon by Gasification with CO_2-II. The Role of Catalytic Impurities," Carbon, 9, (1971), 63.

11. Riede, Bruce E. and Deran Hanesian, "Kinetic Study of Graphite-Steam Reaction", Industrial Engineering Chemistry: Process Design Development, 14, (1975), 70.

12. Schechter, R.S. and J.L. Gidley, "The Change in Pore Size Distribution From Surface Reactions in Porous Media," AIChE Journal, 15, (May 1969) 339.

13. Smisek, Milan and Slavoj Cerney. Active Carbon. Amsterdam: Elsevier Publishing Co., 1970.

14. Strickland, R.F., "Interaction of Steam and Charcoal at Low Pressures," Proceedings of Royal Society of London, 189, (March 1947), 1.

15. Thomas, W.J., "The Effect of Oxidation on a Pore Structure of Some Graphitized Carbon Blacks," Carbon, 3, (1966), 435.

16. Walker, Philip L. Chemistry and Physics of Carbon. Volume 1. New York: Marcel Dekker, Inc., 1971.

17. Walker, P.L. and M. Kawahata, "Mode of Porosity Development in Activated Anthracite, "Proceedings from the Fifth Carbon Conference, 2, (1962), 251.

18. Wen, C.Y., "Noncatalytic Heterogeneous Solid Fluid Reaction Models," Industrial Engineering Chemistry, 60, (1968), 34.

19. West, Ronald E., "Effect of Porous Structure on Carbon Activation," Environmental Protection Agency, Project #17020 DDC Publication, (June 1971).

20. Yoshikawa, Fumiaki. "Change in the Pore Structure and Adsorption Characteristics of Activated Carbons." Masters of Science, Kyoto University: Kyoto, Japan, (March 1975).

APPENDICES

APPENDIX A

DEVELOPMENT OF THE EQUATIONS FOR THE COMBINED MODELS

The derivation of the slit shaped micropore differential equations from the general population balance equation by Hashimoto and Silveston.[4] The general equation is equation 2.4.

$$\frac{\partial f}{\partial t} + \frac{\partial}{\partial r}\left(f \frac{dr}{dt}\right) - B + D = 0 \qquad 2.4$$

where f is the density distribution function, B is the rate of formation of new pores by initiation and combination, and D is the death term on the rate at which pores coalesce with adjacent pores. Multiplying equation 2.4 by r^n and integrating from 0 to ∞ yields:

$$\frac{\partial M_n}{\partial t} - n\int_0^\infty r^{n-1} \frac{dr}{dt} f \, dr + \int_0^\infty r^n (D-B) dr = 0 \qquad A\text{-}1$$

where the micropore growth is defined by equation 2.5.

$$\frac{dr}{dt} = \frac{K_1 M_B C_g}{\rho_t} \qquad 2.5$$

The birth and death terms are the same as developed by Hashimoto and Miura[3].

$$B = B_c + B_f$$

$$B_f = K_f C_g \rho_{B_i} \delta(r-r_f)$$

$$B_c = \frac{1}{2} \phi_i \int_0^r f(r-r_1) f(r_1) dr_1$$

$$D = \phi_i f(r) \int_0^\infty f(r_1) dr_1$$

where K_f = the initiation rate constant

C_g = reactant concentration

δ = Dirac delta function

r_f = minimum slit spacing

r = slit spacing

The last term in equation A-1 becomes

$$r^n(D-B)dr = \phi_i\int_o^\infty r^n f(r)\int_o^\infty f(r_1)dr_1dr - \frac{1}{2}\phi_i\int_o^\infty r^n\int_o f(r-r_1) f(r_1)dr_1dr - K_fC_g\rho_B\int_o^\infty r^n\delta(r-r_f)dr \qquad A-2$$

The integrand in the last integral of equation A-2 becomes

$$r^n\delta(r-r_f) = r_f^n \qquad A-3$$

because of the slit approximation.

The middle term in equation A-2 can be rearranged to give

$$\int_o^\infty r^n\int_o^r f(r-r_1)f(r_1)dr_1dr = \int_o^\infty f(r_1)\left[\int_o^\infty r^n f(r-r_1)dr\right]dr_1$$

let $r-r_1 = y$, then

$$\int_o^\infty f(r_1)\left[\int_o^\infty (y+r_1)^n f(y)dy\right]dr_1 = \sum_{i=0}^{n}\binom{n}{i} M_iM_{n-i} \qquad A-4$$

Using A-3 and A-4 in A-2 and solving for the moments gives

$$\int_o^\infty r^n(D-B)dr = \phi_iM_oM_n - \frac{1}{2}\phi_i\sum_{i=0}^{n}\binom{n}{i} M_iM_{n-i} - K_fC_g B_i r_f^n \qquad A-5$$

Equations A-5 and 2.5 can be substituted into equation A-1 to give the general moment equation.

$$\frac{\partial M_n}{\partial t} - n\frac{K_1 M_B C_g}{\rho_t} M_{n-1} - K_f C_g \rho_{B_i} r_f^n + \phi_i M_o M_n - \frac{1}{2}\phi_i \sum_{i=0}^{n}\binom{n}{i} M_i M_{n-i} = 0 \qquad \text{A-6}$$

Expanding this for the first two moments gives

$$\frac{\partial M_o}{\partial t} - K_f \rho_{B_i} C_g + \frac{1}{2}\phi_i M_o^2 = 0 \qquad 2.17$$

$$\frac{\partial M_1}{\partial t} - \frac{K_1 M_B C_g}{\rho_t} M_o - K_f C_g \rho_{B_i} r_f = 0 \qquad 2.18$$

Equation 2.17 relates to the micropore surface area and equation 2.18 relates to the micropore volume. The relationship between the moments and the local properties are:

$$S_i = \frac{2 s_i M_o}{\rho_{B_i}} \qquad 2.19$$

$$V_i = \frac{2 s_i M_o}{\rho_{B_i}} \qquad 2.20$$

where S_i = the micropore surface area, this is assumed to be the total measurable surface area

V_i = the micropore volume

s_i = the surface area of one plane in the crystallite

ρ_{B_i} = the micropore apparent density, defined by equation 2.15

Applying equation 2.19 to equation 2.17 yields

$$\frac{\rho_{B_i} dS_i}{2 s_i dt} + \frac{S_i d\rho_{B_i}}{2 s_i dt} - K_f C_g \rho_{B_i} + \frac{1}{2}\phi_i \frac{S_i^2 \rho_{B_i}^2}{4 s_i^2} = 0 \qquad \text{A-7}$$

from equation 2.14, you can obtain

$$d\rho_{B_i} = -\rho^{c}_{B_i} dx_i \qquad \text{A-8}$$

and solving for the dimensionless surface area, $\Gamma = S_i/S_i^{\circ}$, equation A-7 yields equation 2.21

$$\frac{d\Gamma_i}{dt} = \frac{\Gamma_i}{(1-x_i)}\left(\frac{dx_i}{dt}\right) + B_3 - B_4 \Phi_i^{*} \Gamma_i^{2}(1-x_i) \qquad 2.21$$

Doing the same to equation 2.18 yields equation 2.22

$$\frac{dx_i}{dt} = (B_1 \Gamma_i + B_2)(1-x_i) \qquad 2.22$$

where $B_1 = K_i C_g^{\frac{1}{2}} M_B S_i^{\circ}$,

$B_2 = 2.0 r_f s_i \rho_t K_f C_g^{\frac{1}{2}}$

$B_3 = 2.0 s_i K_f C_g^{\frac{1}{2}}/S_i^{\circ}$,

$B_4 = \rho^{\circ}_{B_i} S_i^{\circ} \phi_i^{\circ}/4.0 s_i$,

$\Phi_i^{*} = \phi_i/\phi_i^{\circ} = 1/(1-x_i)^{n_i}$,

The macropore equations are similar to the equations developed by Hashimoto and Silveston.[4]

The general moment equation is the same as for the micropores, equation A-1. The macropore growth is

$$\frac{dr_a}{dt} = \frac{K_1 M_B C_g}{\rho_{B_{oa}}} \qquad 2.24$$

This is similar to the micropore growth equation except the wall density is $\rho_{B_{oa}}$, not ρ_t. This means the equation accounts for the presence of micropores and other macropores. The birth term has only one term, B_c. The initiation of macropores was assumed to be negligible. The birth of a pore of radius, r_c, is given by:

$$B_c = \frac{1}{2}\phi_a \int_0^r f(r_c) f(r_1) dr_1 \qquad 2.25$$

r_c is the radius of a new pore created by the coalescence of two other pores. From the assumption of the cylindrical shape, the radius is defined as

$$r_c = \frac{2V_a}{S_a} = \frac{r_1^2 + r_2^2}{r_1 + r_2} \qquad 2.26$$

Hashimoto and Silveston[4] linearized the function as

$$r_c = \alpha (r_1 + r_2) \qquad 2.27$$

where $\alpha = 0.5$ when $r_1 \equiv r_2$ and $\alpha = 1.0$ when $r_1 >> r_2$. The removal of pores due to combination with adjacent pores is

$$D_a = \phi_a f(r) \int_0^\infty f(r_1) dr_1 \qquad 2.28$$

ϕ_a in equations 2.25 and 2.28 is the macropore combination rate function. Substituting 2.24, 2.25 2.27 and 2.28 into A-1 yields

$$\frac{\partial M_n}{\partial t} - n \frac{K_a M_B C_g}{\rho_{B_{oa}}} M_{n-1} + \int_0^\infty r^n \left[\phi_a f(r) \int f(r_1) dr_1 - \frac{1}{2} \phi_a \int_0^r f(r/\alpha - r_1) f(r_1) dr_1 \right] dr \qquad A\text{-}9$$

The last term can be divided into two terms. The first is

$$\int_0^\infty r^n \phi_a f(r) \int_0^\infty f(r_1) dr_1 dr = \phi_a M_o M_n$$

The second term is

$$-\frac{1}{2} \int_0^\infty r^n \phi_a \int_0^r f(r/\alpha - r_1) f(r_1) dr_1 dr$$

This equation was reduced by Hashimoto and Silveston[4] by replacing the upper limit of the inner integral with r/a to obtain

$$\frac{1}{2}\phi_a\int_0^{\infty}\int_{ar_1}^{\infty} r^n f(r/a - r_1)f(r_1)dr\,dr_1$$

which becomes

$$\frac{1}{2}\,a^{n+1}\,\phi_a\sum_{i=0}^{n}\binom{n}{i} M_{n-i}M_i$$

Using these to replace the last term in equation A-9 yields

$$\frac{\partial M_n}{\partial t} - \frac{nK_aM_BC_g}{\rho_{B_{oa}}} M_{n-1} + \phi_aM_oM_n - \frac{1}{2}\alpha^{n+1}\phi_a\sum_{i=0}^{n}\binom{n}{i} M_{n-i}M_i = 0 \qquad \text{A-10}$$

Expanding this for the first three moments yields 2.29, 2.30 and 2.31

$$\frac{dM_o}{dt} + \phi_a\left(1 - \frac{\alpha}{2}\right)M_o^2 = 0 \qquad 2.29$$

$$\frac{dM_1}{dt} - \frac{K_aM_BC_g}{\rho_{B_{oa}}} M_o + (1-\alpha^2)\phi_aM_oM_1 = 0 \qquad 2.30$$

$$\frac{dM_2}{dt} - \frac{2K_aM_BC_g}{\rho_{B_{oa}}} M_1 + (1-\alpha^3)\phi_aM_oM_2 - \alpha^3\phi_aM_1^2 = 0 \qquad 2.31$$

By using the moment relations,

$$M_o = \frac{L_a\rho_{B_{oa}}}{\ell} \qquad 2.32$$

$$M_1 = \frac{S_a\rho_{B_{oa}}}{2\pi\ell} \qquad 2.33$$

$$M_2 = \frac{V_a\rho_{B_{oa}}}{\pi\ell} \qquad 2.34$$

and noting that

$$\frac{\partial \rho_{B_{oa}}}{\rho^{\circ}_{B_{oa}}} = -\left(V_a^{\circ} \rho^{\circ}_{B_{oa}} d\Omega_a + \frac{\rho^{\circ}_{B_{oa}} dx_i}{\rho^{\circ}_{B_i}(1-x_i)^2} \right)(1-x_{oa}) \qquad A\text{-}11$$

Equations 2.29, 2.30 and 2.31 can be solved in terms of the relative macropore length, surface area and volume. This yields equations 2.35, 2.36 and 2.37.

$$\frac{d\Lambda_a}{dt} = \Lambda_a \left[B_5 \left(\frac{d\Omega_a}{dt}\right) + \frac{B_6}{(1-x_i)^2}\left(\frac{dx_i}{dt}\right)\right](1-x_{oa}) - \left(1 - \frac{\alpha}{2}\right) \qquad 2.35$$
$$B_9 \Phi_a^* \Lambda_a (1-x_{oa})$$

$$\frac{d\Gamma_a}{dt} = \Gamma_a \left[B_5 \left(\frac{d\Omega_a}{dt}\right) + \frac{B_6}{(1-x_i)^2}\left(\frac{dx_i}{dt}\right)\right](1-x_{oa}) + \frac{B_8 \Lambda_a}{(1-x_{oa})} - \qquad 2.36$$
$$2\pi(1-\alpha^2) B_9 \Phi_a^* \Lambda_a \Gamma_a (1-x_{oa})$$

$$\frac{d\Omega_a}{dt} = \frac{\Omega_a}{(1-B_5(1-x_{oa})\Omega_a)}\left[\frac{B_6(1-x_{oa})}{(1-x_i)^2}\right]\left(\frac{dx_i}{dt}\right) + \frac{B_7 \Gamma_a}{B_5(1-x_{oa})(1-B_5(1-x_{oa})\Omega_a)} -$$
$$\frac{(1-\alpha^3) B_9 \Phi_a^* \Lambda_a \Omega_a (1-x_{oa})}{(1-B_5(1-x_{oa})\Omega a)} + \frac{\alpha^3 B_9 S_a^{\circ 2} \Phi_a^* \Gamma^2 (1-x_{oa})}{4\pi L_a^{\circ} V_a^{\circ}(1-B_5(1-x_{oa})\Omega_a)} \qquad 2.37$$

where $B_5 = V_a^{\circ} \rho^{\circ}_{B_{oa}}$, $B_6 = \rho^{\circ}_{B_{oa}} / \rho^{\circ}_{B_i}$

$B_7 = K_a M_B C_g^{\frac{1}{2}} S_a^{\circ}$, $B_8 = 2.0\pi K_a M_B C_g^{\frac{1}{2}} L_a^{\circ} / S_a^{\circ} \rho^{\circ}_{B_{oa}}$

$B_9 = \phi_a^{\circ} L_a^{\circ} \rho^{\circ}_{B_{oa}} / \bar{l}_a$

$\Phi_a^* = \phi_a / \phi_a^{\circ} = 1/(1-x_{oa})^{n_a}$

APPENDIX B

EQUIPMENT SPECIFICATIONS

REACTOR

Material - Quartz Glass
ID1 = 5.4cm OD1 = 5.85cm
ID2 = 3.5cm OD2 = 3.97cm
Inner Length = 43 cm
Outer Length = 50 cm
Length to Outlet = 39.5 cm
Length to Inlet = 35 cm

FURNACE

Type - Electrical Resistance
Kilowatts - 3.2
Volts - 100
Amps - 32
Maximum Temperature - 1000°C

TEMPERATURE CONTROLLER

Producer - Chino
PID Solid State Controller

TEMPERATURE RECORDER

Producer - Chino
No. of Points - 6
Range - Lowest 0-650°C
Highest 600-1200°C

MICRO-BALANCE

Producer - Shinko Denshi Co. Ltd.
Range - 0.25-2.5 gm
Sensitivity - 0.5 mg
Chart Speed - 2-60 cm/hr

WEIGHT RECORDER

Producer - Yokogawa
Range - 0.5mv-100v
Sensitivity - 0.5 mg
Chart Speed - 2-60 cm/hr

MICRO TUBE PUMP

Producer - Toyko Rikakikai Co. Ltd.

DEOXYGEN UNIT

Length - 40 cm
ID = 4 cm
OD = 5 cm
Temperature - 175°C

SAMPLE BASKET

Material - Platinum Mesh
Mesh Size - 48 x 64 Tyler
Depth - .55 cm
Diameter - 1.45 cm

ROTAMETERS

Calibrations - for N_2 at 20°C
and 760mm of Mercury
Range - 50-1000 cc/min

APPENDIX C

CALCULATION OF THE EFFECTIVENESS FACTOR

An effectiveness factor for the micropores is calculated for the pelletized material at the highest reaction rate to determine if diffusional resistances are a problem.

An effectiveness factor is defined by

$$\eta_a = 3/K^2(K \coth (K) - 1)^* \qquad C\text{-}1$$

where $K = \sqrt{K_s a/D_a}\ R$

K_s = surface rate constant

a = surface area to volume ratio

D_a = effective diffusivity

R = particle radius

The surface reaction rate in a single pore is

$$\frac{dr}{dt} = \frac{K_s M_B C_g}{\rho_t} \qquad 2.5$$

The relationship between the radius and volume is

$$V_i = r_i S_i \qquad C\text{-}2$$

so

$$dr_i = \frac{dV_i}{S_i} \qquad C\text{-}3$$

The micropore volume can be related to the micropore conversion, to give

$$dr_i = \frac{dx}{S_i \rho^\circ_{B_i}(1-x_i)^2} \qquad C\text{-}4$$

*Bird, Stuart and Lightfoot. Transport Phenomena. John Wiley and Sons, Inc. p. 545.

Combining this with equation 2.5 and rearranging, yields an expression for the surface rate constant, which at the initial conditions becomes

$$K_s = \frac{\left(\frac{dx}{dt}\right)_o \rho_t}{M_B C_g S_i^\circ \rho_{B_i}^\circ} \qquad C\text{-}5$$

Four different particle radii were used with the pelletized material. All except the largest had approximately the same reaction rate. Therefore, their effectiveness factors should be close to one.

The highest reaction rate was at 850°C, 1 atm. partial pressure of steam. This is shown in Figure 4.3, p. 51. Using this rate and equation C-5, the effective surface rate constant can be calculated

$$K_s = 4.38 \times 10^{-7} \text{ cm/sec}$$

The surface area to volume ratio, a, is

$$a = S_i^\circ \rho_{B_i}^\circ = 7.22 \times 10^6 \text{ cm}^2/\text{cm}^3$$

The smallest particle had a radius of 0.0273 cm and assuming that this particle has an effectiveness factor very close to one ($\eta_e \approx 0.98$ to 0.99), effective diffusivity, D_a, can be calculated. For $\eta_e = 0.98$, K from equation C-1 equals 0.6 and the effective diffusivity, D_a, equals 0.00655 cm^2/sec. Using these values with the other particle radii the effectiveness factors were calculated. This was repeated for an effectiveness factor of 0.99 for the smallest particle. The values are summarized in Table C-1.

TABLE C-1

EFFECTIVENESS FACTORS FOR THE PELLETIZED MATERIAL

R_p (cm)	K	D_a cm^2/sec	η_e
0.0273	.6	.00655	0.98
0.0325	.72	.00655	0.97
0.0538	1.18	.00655	0.92
0.110	2.42	.00655	0.75
0.0273	.4	.0147	0.99
0.0325	.48	.0147	0.98
0.0538	.79	.0147	0.96
0.110	1.61	.0147	0.86

APPENDIX D

SCANNING ELECTRON MICROGRAPHS

Electron Scanning Electron Micrographs of the initial coal char samples. Each was Gold-Palladium coated.

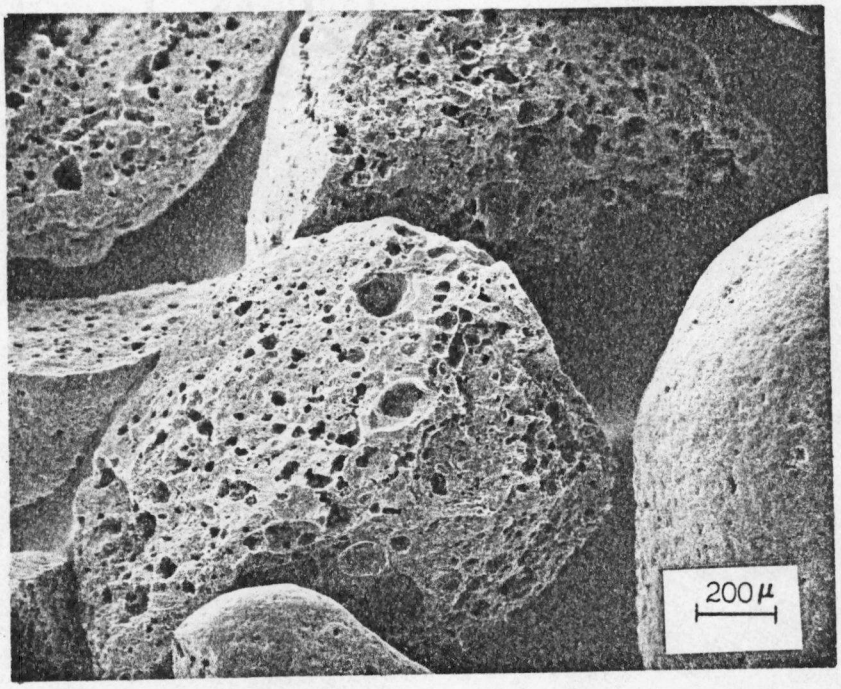


Figure D-1. Micrograph of the Pelletized Material at 50x.

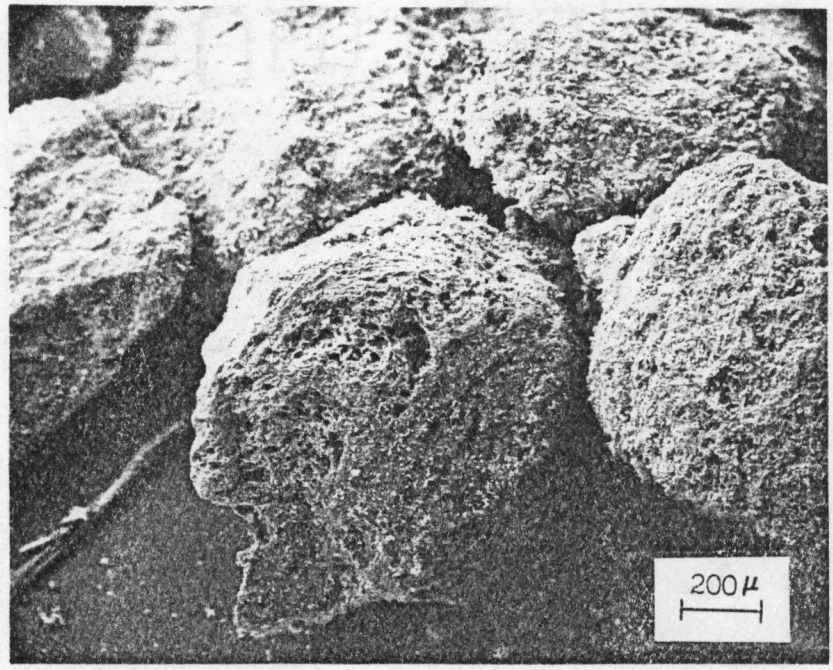


Figure D-2. Micrograph of the Non-Pelletized Material at 50x.

VITA

Bruce Edwin Murphree was born in Memphis, Tennessee on June 13, 1952. He attended elementary school in West Memphis, Arkansas and Milan, Tennessee. He graduated from Milan High School in 1970. In the summer of the same year he entered The University of Tennessee, Knoxville and received a Bachelor of Science degree in Chemical Engineering in August, 1975.

During his undergraduate education, he was in the Cooperative Education Program and was employed by E.I. DuPont at their Savannah River Plant, Aiken, South Carolina.

After receiving his bachelor's degree, he entered the Graduate School of The University of Tennessee, Knoxville. He entered a new program at The University of Tennessee in which one conducts his course work at The University of Tennessee and his research at a Japanese University. In January, 1976, he received a scholarship from the Japanese Ministry of Education to fund his thesis research in Japan, from January 1976 through March 1977. He conducted his research at the Department of Chemical Engineering, Kyoto University, Kyoto, Japan under the supervison of Professor Kenji Hashimoto.

He is a member of Phi Sigma Kappa, Alpha Chi Sigma, Tau Beta Pi, Phi Kappa Phi, and the American Institute of Chemical Engineers. After graduation he will be employed with E.I. DuPont, Savannah River Laboratory, Aiken, South Carolina.